Observation of heavy cosmic-ray primaries over the wide energy range from ~100 GeV/particle to ~100 TeV/particle: Is the celebrated "knee" actually so prominent?

Masakatsu Ichimura, Masataka Kogawa, Shuichi Kuramata, Hiroyuki Mito, Takayuki Murabayashi, Hirotada Nanjo, Takahiro Nakamura, Katsuyuki Ohba, Tatsumi Ohuchi, Tomohiko Ozawa, and Yoshiyuki Yamada
Department of Physics, Hirosaki University, Bunkyo-cho 3, Hirosaki, Aomori, Japan

Hideya Matsutani
Faculty of Medicine, Hirosaki University, Hirosaki, Aomori, Japan

Zenjiro Watanabe
Aomori University, Aomori, Japan

Eiji Kamioka, Keisuke Kirii, Motoyasu Kitazawa, Tadashi Kobayashi, Atsusi Mihashi, Toru Shibata, and Kazuo Shibuta
Department of Physics, Aoyama Gakuin University, Chitosedai 6-16-1, Setagaya, Tokyo, Japan

Hisahiko Sugimoto
Syonan Institute of Technology, Fujisawa, Kanagawa, Japan

Kazuma Nakazawa
Physics Department, Gifu University, Yanagido, Gifu, Japan
(Received 2 December 1992)

We have exposed a new type of emulsion chamber of area 1.53 m^2 at an atmospheric depth of 11.7 g/cm^2 for 22.2 h. The chamber makes extensive use of screen-type x-ray films, which have recorded the tracks due to over 100 000 cosmic-ray heavy primary nuclei of $Z \gtrsim 8$. With this experiment we have succeeded in determining the absolute intensities of the heavy primaries over a pretty wide energy range from a few GeV/nucleon up to ~1 TeV/nucleon, using a single detector and a unified charge-and-energy determination method. In the present paper we give a report of our results on silicon and heavier components, accompanied by a detailed account on our newly adopted energy determination method and a discussion of its accuracy. Our iron flux is in agreement with that obtained by Spacelab-2, the integral spectral index β being nearly constant, ~1.5, up to a few TeV/nucleon. Of peculiar interest is our silicon flux, which is again consistent with the Spacelab-2 result. The energy spectrum gets softer beyond 100 GeV/nucleon, β being as high as ~1.95 there. Current interstellar acceleration and propagation models will meet difficulty in explaining this result. We also report about the abundance ratio of the subiron group to iron, which is strongly sensitive to the escape length of cosmic rays in the Galaxy, and find that it decreases in the form of power laws over the wide energy range from a few GeV/nucleon to a few TeV/nucleon, though a quantitative study in connection with a particular propagation model is reserved to the future. Our all-particle spectrum deviates significantly from that of the proton satellites beyond 50 TeV/particle, while both agree rather well with each other in the lower energy range. When we investigate individual heavy components, we find that all their respective fluxes multiplied by $E_P^{2.5}$ (E_P is the primary energy per particle) show a decreasing tendency around ~10 TeV/particle and beyond, no indication of recovery being observed as the energy gets even higher. This means that the heavy components, paricularly iron, do not increase so drastically as to cover the excess in the "knee" region. Extrapolation of our all-particle spectrum up to 10^{15}–10^{16} eV/particle indicates a milder "knee" shape than that found by the air shower experiments. If the break is as sharp as hitherto reported, then it will suggest either (i) there is a sharp break which might be due to a drastic advent of new components (other than heavy primary nuclei), or a drastic change in nuclear interaction, or (ii) the break just appears to be sharp due to a ~20% (or more) systematic overestimation in converting the air shower sizes into the primary energy values in the "knee" region.

PACS number(s): 96.40.De

I. INTRODUCTION

The composition and energy spectra of cosmic-ray primaries brings us valuable information on the nature of cosmic-ray sources, the acceleration mechanisms, and the propagation in the interstellar medium. Study [1] on the mechanism of shock acceleration predicts naturally a powerlike behavior for the particle rigidity at the source,

$R^{-2-\delta}$, where δ is expected to be 0.1–0.3 depending on the shock strength, though difficulty still remains above the "knee" region. The difference between the power index at the source and at the Earth gives us information on the propagation mechanism in the interstellar medium. Therefore, a separate observation of the respective primary spectra for various elements is highly desirable.

Though precise *direct* measurements have been performed with the use of balloons and satellites, and a considerable amount of data has been accumulated at low energy region $\lesssim 10$ GeV/nucleon (hereafter denoted GeV/N), it is not straightforward to deduce cosmic-ray behavior at the source in this energy region. This is because many effects such as solar modulation, ionization loss, energy-dependent cross sections for nuclear-spallation processes, etc., must be corrected for in constructing a source model from the observational data after propagational modification. Hence one inevitably looks for observations at higher energies where the uncertainties in these effects can be neglected.

Until now the highest-energy data obtained *directly* with smallest statistical uncertainty has come from the proton-satellite experiment [2], giving the all-particle spectrum extending up to somewhere above $\sim 10^{15}$ eV/particle, overlapping with the energy of air shower experiments. It is, however, difficult to get the separate respective spectra for individual elements. In particular, the proton spectrum, the most dominant component in the all-particle spectrum, is uncertain due to several problems, for instance, chamber efficiency estimation, charge resolution of primaries, etc. We are also concerned that an energy calibration on accelerators has never been reported.

For the proton spectrum, passive experiments depending on the use of the balloon-borne emulsion chambers are more readily achievable, and several groups have obtained data, including JACEE [3] and ourselves [4]. In principle, we can estimate any size of shower energy ΣE_γ initiated by a proton interaction with considerable accuracy [5] as long as the thickness of the calorimeter is large enough to catch the shower maximum, and the only problem we worry about is the fluctuation in k_γ, the energy fraction transferred to γ rays ($\pi^0 \rightarrow 2\gamma$), when converting ΣE_γ to the primary energy of the shower-inducing proton $E_0 (= \Sigma E_\gamma / k_\gamma)$.

Heavy components have been explored by HEAO-3 [6] and recent Spacelab-2 [7] experiments and they are excellent in the resolution of both the charge and the energy of the primaries, and have brought us precious data for the abundance ratio in the high-energy region 10–100 GeV/N and beyond. It is remarkable that the latter group has given the iron energy spectrum reaching up to ~ 100 TeV/particle.

We have been performing balloon-borne emulsion chamber experiments in Japan since 1987. Let us summarize the flight situation in Table I. In the first two experiments [4,8] (1987 and 1988), we exposed orthodox calorimeter-type emulsion chambers (the 1988 calorimeter was slightly reduced in order to test a new type of sensitive material) with results reported in Refs. [4,8], respectively. In these two experiments we obtained data for the proton and helium components over the range from 5 to 100 TeV/N, though the statistical significance of the helium data is rather poor.

We have found through these earlier experiments that there exists inevitable difficulty in the energy resolution for heavy components, in addition to the problem of poor statistics. Indeed, we can estimate the energy flow released into the electromagnetic component ΣE_γ with sufficient accuracy even in the case of an iron-initiated cascade shower [5]. However, it is not straightforward to convert ΣE_γ to the *primary energy* E_0 since very large fluctuation is involved in the conversion process. The sources of fluctuations are as follows: (i) The outcome of a nucleus-nucleus collision differs widely depending on the impact parameter; (ii) both the inelasticity and the charged-to-neutral energy sharing distribute very broadly in individual constituent nucleon-nucleon collisions; (iii) the behavior of the resultant electromagnetic cascade showers fluctuate very widely around the *average* one, used in converting the shower sizes into ΣE_γ. Those fluctuation effects may very well accumulate up to a factor of ~ 100, unless the calorimeter has enough material thickness to convert all the incident kinetic energy into electron showers.

We have constructed a new type of emulsion chamber, based on our preparatory experiment showing that a chamber equipped with multilayered screen-type x-ray films (SXF's) is quite efficient for heavy primary cosmic-ray observations [8,9]. The decisive point in which our chamber differs from the orthodox calorimeter-type one is the absence of the calorimeter module. The absence

TABLE I. Flight situation, and remarks on each experiment.

Chamber Number	I	II	III	IV
Launch date	May 25, 1987	May 28, 1988	May 25, 1989	May 28, 1991
Exposure time (h)	31.1	19.7	22.2	15.8
Chamber area (m^2)	0.4	0.31	1.53	1.22
Altitude (g/cm^2)	32.8	19.4	11.7	8.9
Weight (kg)	250	200	200	150
Main elements	p,α	p,α	Heavy	Heavy
Energy region (TeV/N)	8–100	4–50	0.04–1	0.1–1
Calorimeter	Orthodox	Reduced	None	None
Gondola direc.				Controlled

means that we have got rid of the heavy lead absorber of the calorimeter, enabling us to construct a chamber of larger area and lower weight, which in turn makes it easier to catch higher-energy heavy primaries. The present paper is focused on giving the results obtained in our recent experiment in 1989, the first one depending on the use of our new-type chamber.

The observation of heavy cosmic-ray primary with use of our new type of emulsion chamber has been discussed in detail in Ref. [9]. We only briefly discuss the experimental method in Sec. II, but show at some length in Sec. III how the primary energy is determined. In Sec. IV we go into detail on the process to convert the observed data to the absolute intensity at top of the atmosphere, because our observation level is ~ 10 g/cm^2, where the atmospheric correction is quite important. In Sec. V, we present the experimental data and compare it with those obtained by other groups in the past, and we discuss the all-particle spectrum in connection with air shower data as well as the proton-satellite data.

II. EXPERIMENTAL PROCEDURE

A. Flight situation and chamber structure

On May 25, 1989, we launched a balloon loaded with the new type of emulsion chamber from the Sanriku Balloon Flight Center, Japan. The total exposure time was 22.2 h and the average level reached was 11.7 g/cm^2. After the recovery of the chamber, the sensitive materials were processed as quickly as possible. The detailed accounts of processing are given in Ref. [9].

We illustrate the chamber structure in Fig. 1. Our chamber consists of two modules: a trigger layer module and a jet detector module. The latter is designed to measure simultaneously the emission angle of fragment particles produced by nucleus interaction; i.e., it plays also a role of jet analyzer. Total area of the chamber S is 1.53 m^2, composed of ten equal units, each having the area 35.5×43.0 cm^2. Total thickness of the chamber is 4.81 cm in geometrical length, and 15.5 g/cm^2 in material thickness.

Our chamber has a pretty large $S\Omega_{\rm geom}$, where $\Omega_{\rm geom}$ stands for the geometrical solid angle of our chamber for cosmic-ray detection. Especially, $S\Omega_{\rm geom}=4.81$ m^{2}sr for our 6.19-mm-thick trigger layer module. Our large $S\Omega_{\rm geom}$ is partly due to our $\Omega_{\rm geom}$, amounting to $\sim\pi$ sr, which in turn is due to the sensitivity of screen-type x-ray film (SXF) which does not drop for inclined tracks. It is to be compared with CR-39, which has a severe detection bias against the tracks of larger inclination. For instance, if we set the detection limit inclination angle $\theta_{\rm max}$ to be $\sim 45°$, we have $\Omega_{\rm geom}\sim\pi/2$ sr.

Our large $S\Omega_{\rm geom}$ has brought us over 10^5 tracks due to heavy primaries of $Z\gtrsim 8$, although the flight duration of our balloon was not too long.

B. Search for nucleus interaction

Illustrated in Fig. 2 is (a) a photograph of SXF taken from a TV monitor connected with a charge coupled device (CCD) camera, and (b) a three-dimensional darkness contour map corresponding to the photograph. One can easily find with the naked eye the tracks of primary cosmic-ray nuclei not lighter than oxygen recorded on SXF.

If the track-producing heavy primary makes a collision with a nucleus of the chamber material, the darkness of the track spot on SXF shows an abrupt change. When the collision ends up with a small multiplicity event, the track spot is to disappear on the subsequent SXF sheets. On the other hand, if it leads to a high-energy high-multiplicity event, for example, with $\gtrsim 100$ collimated high-energy secondaries, the darkness of the SXF spot is to show a sudden increase just after the interaction, followed by a rapid attenuation on the deeper SXF sheets, reflecting the spreading out of the secondary tracks. The attenuation of the spot darkness depends of course on the

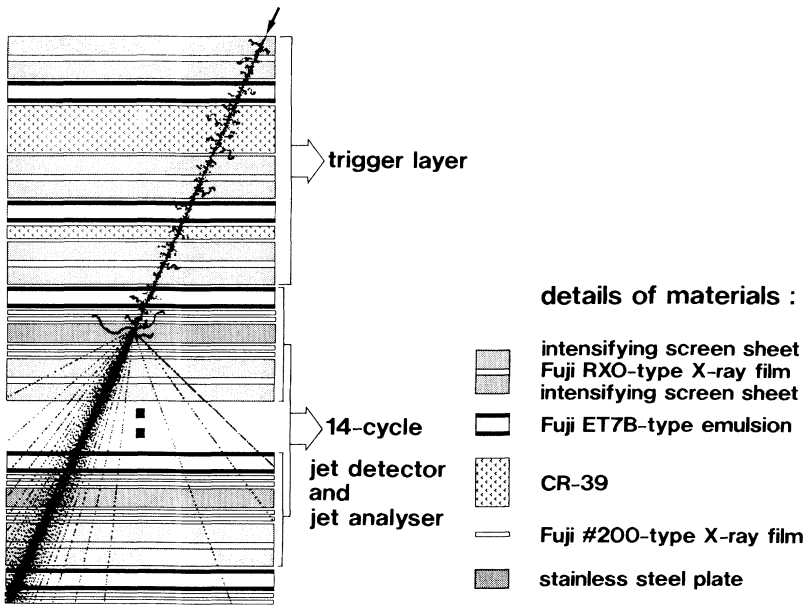

FIG. 1. Illustration of our chamber structure.

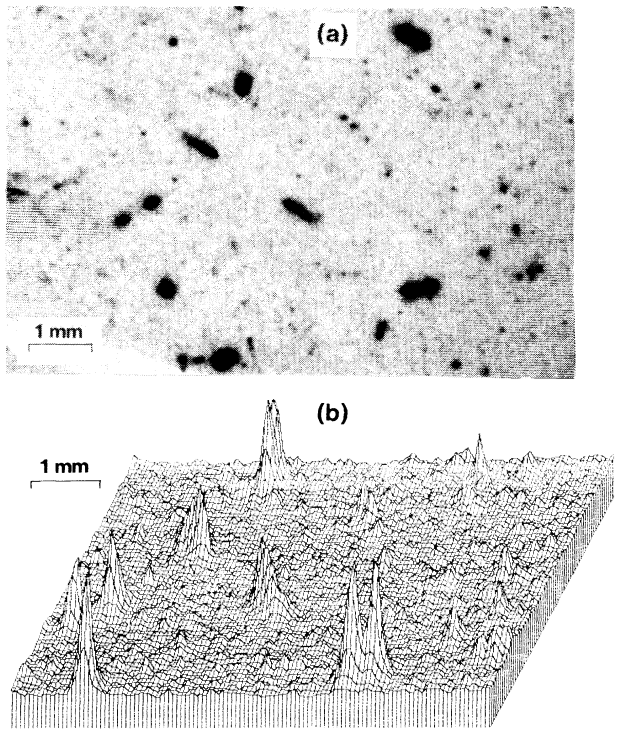

FIG. 2. Photograph of cosmic-ray heavy primaries recorded on x-ray film, (a) taken from the TV monitor and (b) the three-dimensional darkness contour map corresponding to the photograph.

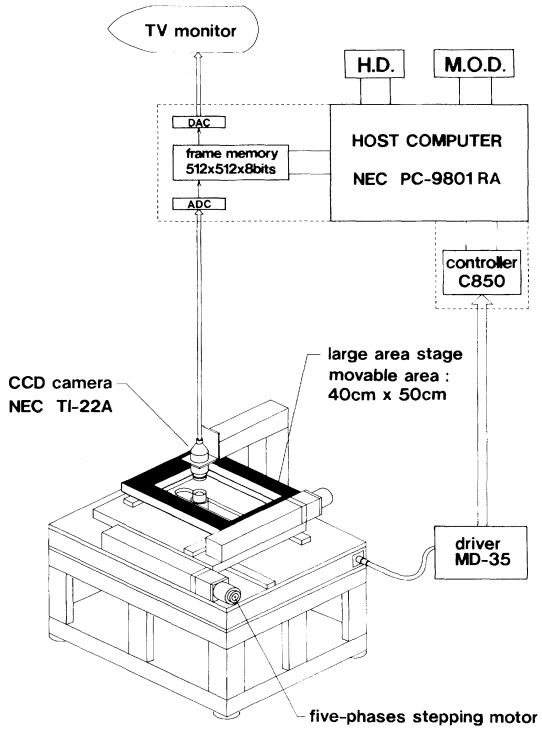

FIG. 3. Illustration of our scanning system to search automatically for heavy cosmic-ray tracks recorded on x-ray film.

interaction energy.

Though we can easily detect with the naked eye the vertex point of the nucleus interaction on SXF, it is hard to complete the detection of numerous signals without miss. Hence, we made an autoscanning system incorporating a CCD camera with a movable area of 40×50 cm^2. We demonstrate in Fig. 3 the outline of this system, which makes the search for vertex point on SXF quite speedy and accurate.

The x-y coordinate and the optical darkness of each track spot on SXF are saved in hard-disk memory during the autoscanning work, so that we can immediately get both the zenith and azimuthal angles of arriving cosmic-ray nuclei as well as its ionization (see next subsection). The zenith angle of each primary is independently obtained by the use of a double-sided nuclear emulsion plate inserted together in the jet detector, though the work is somewhat hard because it involves microscopic measurements. We found the two methods are in accord with each other within a few percent [10].

We summarize in Table II the number of the heavy primary tracks accompanied by local interactions in our chamber detected by this scanning system, where "total tracks" include those colliding in the trigger layer.

C. Charge determination

Since the optical darkness of each track spot on the x-ray film reflects the charge of the incident heavy primaries, we present a scatter plot of the darkness versus the zenith angle in Fig. 4, where we plot only those passing through the trigger layer. The energy of almost every track-producing heavy primary is larger than 4.03 GeV/N, the effective geomagnetic cutoff energy at Sanriku latitude with $[N,E]=[39.16°,141.83°]$.

In the figure we find several densely populated zones, which are to correspond to primary even-even nuclei such as iron, silicon, and so on. Absolute charge calibration has been performed by the δ-ray counting method with the use of the nuclear emulsion plate [11]. Unfortunately, CR-39 was of no service for our present charge calibration, although we also inserted CR-39 layers within our trigger layer module (see Fig. 1). This is be-

TABLE II. Total track number detected in our chamber, and the number of nuclear interactions occurred within jet detector layer (see also Fig. 1).

Total tracks recorded on x-ray film: 102 536		
Total events of nuclear interaction occurred in the jet detector layer: 28 517		
Charge range	Primary	Event number
7.5–8.5	Oxygen	4579
9.5–10.5	Neon	4599
11.5–12.5	Magnesium	5798
13.5–14.5	Silicon	4010
15.5–16.5	Sulfur	1091
17.0–25.0	Sub-iron	5263
≥25.0	Iron group	3177

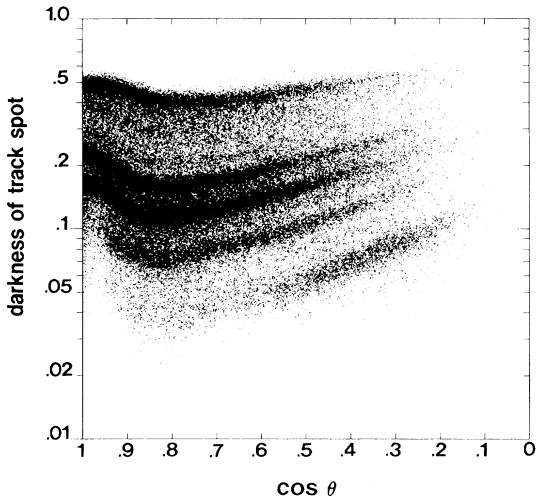

FIG. 4. Scatter plot of spot darkness vs $\cos\theta$, obtained by the autoscanning system.

cause the surface of the CR-39 layers after processing turned out to be in very poor condition with deformed etch-pit cones.

Next in the figure, one observes that each densely populated zone has an upward concave form, with minimum at $\cos\theta \sim 0.85$. The decrease in darkness with θ for $\cos\theta \gtrsim 0.85$ is due to separation between the constituent dark spots of each double spot pair on either side of SXF, the measuring slit ($100 \times 100\ \mu m^2$) of the CCD becoming unable to cover the whole of the pair as θ increases. On the other hand, the increase in darkness with θ for $\cos\theta \lesssim 0.85$ is caused by the increase in number of the scintillation photons, as the primary nucleus with a larger θ has a longer path length within the intensifying screen layer.

A detection bias exists against lighter elements such as oxygen and neon in the small zenith-angle region. That is because a lower Z nucleus with nearly vertical incidence leaves only small SXF dark spot signals, which are sometimes difficult to identify out of the swarming background noise dark spots. We are, however, free from such bias for the elements not lighter than silicon.

On the basis of Fig. 4, after taking the zenith-angle dependence of the spot darkness into account, we can obtain the charge histogram [9,10] as shown in Fig. 5, where we have added the Gaussian curves, one for each element of Z from 15 (phosphorus) up to 25 (manganese), which, all put together, reproduce the observational data best. Each Gaussian curve has been obtained in the following way.

First, as it is known that elements with $Z \geq 27$ are far less abundant than iron in cosmic rays, it would be quite safe to get the standard deviation σ_{26} of the iron charge-estimate distribution from the observational one in its larger tail. We get σ_{26} to be 0.97 charge unit in this way. Next, the observational distribution shows that silicon has a conspicuous enough peak, so that we would be allowed to get σ_{14} from the shape of the observed distribution around the Si peak. Thus we get σ_{14} to be 0.46 charge unit. Now, for $15 \leq Z \leq 25$, the most natural guess for σ_Z would be that it is a monotonically increasing function of Z. For our practical purpose, the formula

$$\sigma_Z = \sigma_{14} + \frac{Z - Z_{14}}{Z_{26} - Z_{14}}(\sigma_{26} - \sigma_{14})$$
$$= 0.46 + \frac{Z - 14}{12} 0.51 \qquad (1)$$

has been tentatively used. Having σ_Z's as above, the only parameters open to adjustment are the peak heights, and they are uniquely given by the least-squares method, under the constraint that the sum of the areas under the Gaussian curves reproduce the observational data best [12].

One might not feel comfortable enough, on the fear

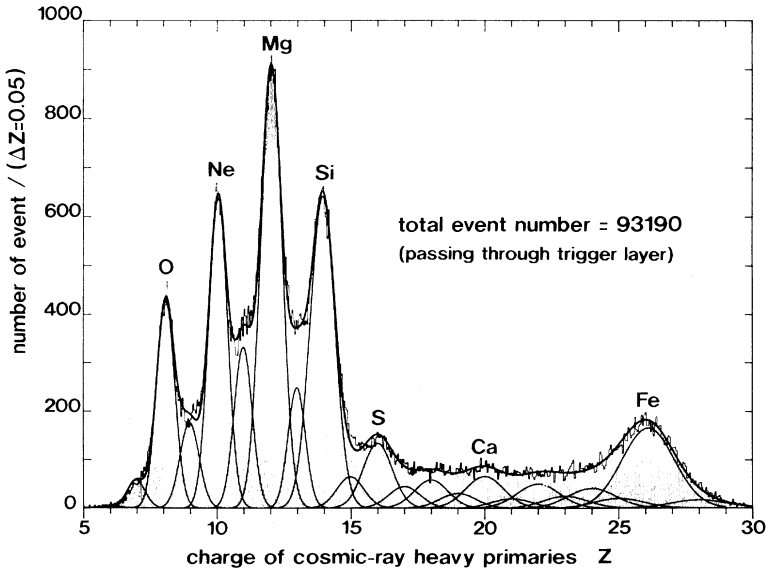

FIG. 5. Charge spectrum of heavy cosmic-ray primaries passing through the trigger layer. The height of histogram does not always correspond to the intensity of each element, because of detection-loss bias for light elements with small zenith angle.

that there might be also some systematic effect such as non-Gaussian tails in each constituent distribution. One support [12,13] of our deconvolution procedure comes from the comparison of our result with HEAO-3 data. Integrating over the individual Gaussian curves, our deconvolution gives the separate intensities of the $15 \leq Z \leq 25$ primaries with $E_0 \geq 4.03$ GeV/N (effective geomagnetic cutoff energy), and the intensities of sulfur, argon, and calcium are in good accordance with the HEAO-3 data [36].

Further support has come from our 1991 balloon experiment. With the help of the azimuthal direction control system on that balloon (see Table I), we have succeeded in estimating the separate intensities of $15 \leq Z \leq 25$ primaries in the range 2 GeV/$N \lesssim E_0 \lesssim 15$ GeV/N, by our deconvolution procedure and the use of the east-west asymmetry effect. Our result is again in good accord with the HEAO-3 data, the details of which are given in Ref. [13].

In Table III, we summarize σ's for even nuclei, and the rate $\nu = N_{\rm obs}/N_{\rm tot}$, where $N_{\rm obs}$ is the observed number of primary with the charge range $Z_{\rm min} \sim Z_{\rm max}$, and $N_{\rm tot}$ the total number integrating over the fitting curve for Z_0 group ($Z_0 \equiv$O, Ne, Mg, . . .). ν is necessary for the estimation of the true number of primary Z_0 at the chamber top [see Eq. (20)]. We further show in the table the purity P for the charge range $Z_{\rm min} \sim Z_{\rm max}$. In the following we summarize the definition of variables mentioned here:

$$N_{\rm obs}(Z_0;Z_{\rm min},Z_{\rm max}) = \sum_{Z_{\rm min} \leq Z < Z_{\rm max}} \Delta N_{\rm obs}(Z) , \tag{2a}$$

$$N_{\rm fit}(Z_0;Z_{\rm min},Z_{\rm max}) = N_{\rm tot} \int_{Z_{\rm min}}^{Z_{\rm max}} e^{-(Z-Z_0)^2/2\sigma^2} \frac{dZ}{\sqrt{2\pi}\sigma} , \tag{2b}$$

$$P(Z_0;Z_{\rm min},Z_{\rm max}) = \frac{N_{\rm fit}(Z_0;Z_{\rm min},Z_{\rm max})}{N_{\rm obs}(Z_0;Z_{\rm min},Z_{\rm max})} , \tag{2c}$$

where $\Delta N_{\rm obs}(Z)$ denotes the observed number within the charge range $(Z, Z+\Delta Z)$.

One finds from Table III that the purity for argon and calcium is of the magnitude $\sim$70%, and those for the other sub-Fe elements such as titanium and chromium are rather poor. It is, however, quite satisfactory for the superposed groups, $17 \leq Z \leq 25$, $21 \leq Z \leq 25$, . . . , etc., showing much better than 80% purity.

Among the primaries passing through the trigger layer, we detected 28 517 nucleus interactions which occurred inside the chamber, and in this paper we present the experimental results for silicon and heavier primaries.

III. ENERGY DETERMINATION

A. Reduced angle

When a high-energy projectile nucleus interacts with a target nucleus, many fragments (p,α,Li, . . .) are produced, and multiple meson production also occurs if the energy is high enough. Kaplon *et al.* [14] remarked on the α fragment among those produced, and determined the projectile energy using the fact that the transverse momentum of α is nearly constant, called "α-opening-angle method." Sato *et al.* [15] applied this method to

TABLE III. Summary of charge resolution σ, purity P, observed number $N_{\rm obs}$, and $\nu = N_{\rm obs}/N_{\rm tot}$ for individual elements.

Primary	σ	$Z_{\rm min}-Z_{\rm max}$	Purity(%)	$N_{\rm obs}$	$\nu = N_{\rm obs}/N_{\rm tot}$
O	0.337	7.5–8.5	94.1	6 705	0.924
Ne	0.349	9.5–10.5	92.7	10 431	0.934
Mg	0.397	11.5–12.5	95.3	15 420	0.853
Si	0.459	13.5–14.5	95.2	11 533	0.780
S	0.545	15.5–16.5	81.5	2 977	0.816
A	0.631	17.5–18.5	66.0	1 663	0.906
Ca	0.716	19.5–20.5	71.4	1 777	0.751
Ti	0.802	21.5–22.5	62.6	1 568	0.778
Cr	0.888	23.5–24.5	45.8	1 790	0.972
Fe	0.974	25.0–28.0	84.9	8 123	1.004
Ni	1.060	27.5–28.5	36.1	947	1.053
Fe-group (Fe+Co+Ni)		25.0–29.0	91.3	9 527	0.955
Sub-Fe group I (Cl+A+K+Ca+Sc +Ti+V+Cr+Mn)		17.0–25.0	90.6	11 754	0.891
Sub-Fe group II (Sc+Ti+V+Cr+Mn)		21.0–25.0	80.5	6 633	1.001
Sub-Fe group III (Cl+A+K+Ca)		17.0–21.0	86.1	7 154	0.977
Sub-Fe group IV (Sc+Ti+V)		21.0–23.0	84.1	3 010	0.785

the cosmic-ray iron primary spectrum by means of a balloon-borne plastic emulsion chamber experiment.

With the α-opening-angle method, the primary energy per nucleon E_0 is given by

$$E_0 \simeq p_0 = \frac{p_{T\alpha}}{\sin\theta_a} \simeq \frac{\langle p_{T\alpha}\rangle}{\theta_\alpha} \quad \text{with } \langle p_{T\alpha}\rangle \simeq 70\text{–}90 \text{ MeV}/c \ , \tag{3}$$

where θ_α is the emission angle of α in the laboratory system and $p_{T\alpha}$ its transverse momentum per nucelon.

Though Eq. (3) is very simple and useful to obtain the primary energy, several problems are inherent from a practical point of view. The first one is the fluctuation of each transverse momentum from the average one, and the second is that the energy is influenced strongly by the most forward α fragment, as found in Eq. (3). The third is the most critical, i.e., the α fragment is not always produced, particularly in the case of a projectile with small mass number such as oxygen ~silicon.

Goldhaber's theoretical speculation [16] is quite useful against these difficulties. Let $\mathbf{p}_f$ be the total momentum of fragment with mass number A_f, produced from the projectile with the mass number A_P. Goldhaber showed that the mean square momentum $\langle p_f^2\rangle$ in the projectile rest frame is given by

$$\langle p_f^2\rangle = \frac{A_f(A_P - A_f)}{A_P - 1}\langle p_N^2\rangle \ , \tag{4}$$

where $\langle p_N^2\rangle$ is the mean square momentum of a nucleon. According to Feshbach and Huang [17], it is approximately related to the Fermi momentum p_F by

$$\sqrt{\langle p_N^2\rangle} = \left[\frac{3}{5}\right]^{1/2} p_F \simeq 180 \text{ MeV}/c \ . \tag{5}$$

Though Eq. (4) is derived from a simple assumption with minimal correlations among nucleon momenta, it reproduces the heavy-ion-beam data on fragment momenta surprisingly well [18].

From Eq. (4), we then immediately obtain the following relation in the form of transverse momentum:

$$\langle p_{Tf}^2\rangle = \frac{A_P - A_f}{A_f(A_P - 1)}\langle p_{TN}^2\rangle \quad \text{with } \langle p_{TN}^2\rangle = \frac{2}{3}\langle p_N^2\rangle \ , \tag{6}$$

where the transverse momentum is expressed as per nucleon. Now let us introduce a variable

$$\Theta = \left[\frac{A_f(A_P - 1)}{A_P - A_f}\right]^{1/2}\theta_f \ , \tag{7}$$

and call it the "reduced angle." Equation (7) means that the angle distribution of fragment particles is independent of the mass of both the projectile A_P and the fragment A_f as long as we use the reduced angle. That is, while the angular distribution, in general, depends on the projectile energy E_0 as well as both masses A_P and A_f, we expect a scaling nature given by

$$\varphi(E_0, \theta_f; A_P, A_f)\, d\theta_f^2 = \varphi(q)\, dq^2$$

$$\text{with } q \equiv \beta_L \gamma_L \Theta \simeq \gamma_L \Theta \ , \tag{8}$$

where β_L and γ_L are the velocity ($c = 1$) of the projectile in the laboratory system and its Lorentz factor, respectively. If we multiply q by M_N (nucleon mass), we can call it the "reduced transverse momentum."

The above consideration indicates that we can treat equivalently any kind of fragments, p, α, Li, Be, . . . , without worrying about no-α-emission types of events. We expect further that the fluctuation of each transverse momentum from the average one [see Eq. (3)] will be reduced considerably, since we use not only α, but also several other kinds of fragments.

B. Comparison with heavy-ion beam

In order to see the validity of the scaling law given by Eq. (8), we show the q^2 distribution of α fragments for various kinds of projectile and many energies obtained by heavy-ion beam experiments [19–22] in Fig. 6. One finds that the scaling nature holds over a wide energy range from a few GeV/N to several hundred GeV/N as well as over the wide mass range from oxygen to iron.

One notes further that its shape may be reproduced by the superposition of two types of Gaussian curves. Thus we fit the following Gaussian functions to the experimental data using the least sum of the squares method ($\tau_1 + \tau_2 = 1$):

$$\varphi(q) = \tau_1 a_1^2 e^{-a_1^2 q^2} + \tau_2 a_2^2 e^{-a_2^2 q^2}$$

$$\text{with } a_{1,2} = M_N/\sqrt{2}\sigma_{1,2} \ , \tag{9}$$

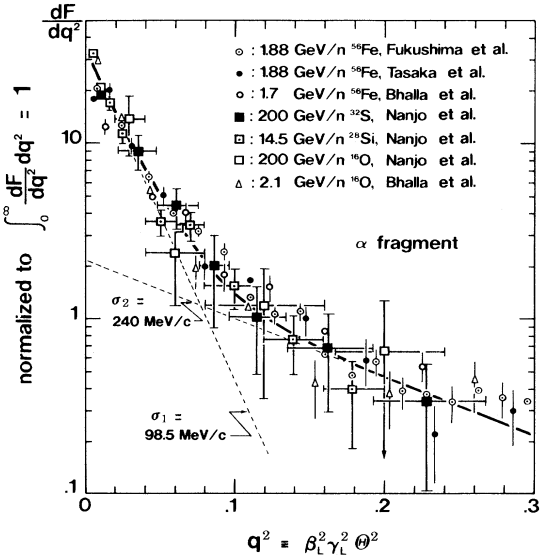

FIG. 6. q^2 distribution of α fragment for various projectiles as well as for several energies. Solid curve is obtained by the superposition of two Gaussian functions with use of the sum of the least-squares method.

where

$$\tau_1=0.7252\ ,\quad \tau_2=0.2748\ , \tag{10a}$$

$$\sigma_1=98.5\ \text{MeV}/c\ ,\quad \sigma_2=239.6\ \text{MeV}/c\ . \tag{10b}$$

In Fig. 6, we draw the fitting curve thus obtained. While σ_1 fitted to the small-angle region is nearly equal to the value 90 MeV/c estimated by Goldhaber [16], we find a rather long tail in the large-angle region. Though several models [19,23] are proposed to explain such a tail, we omit the discussion here because it deviates from the subject of our present paper.

Now, let us calculate the mean value of $\ln q(=\ln\beta_L\gamma_L\Theta)$ with use of Eq. (9):

$$\langle \ln q\rangle=\int_0^\infty \ln q\,\varphi(q)dq^2=-\frac{1}{2}\gamma+\ln\frac{\sqrt{2}\sigma_0}{M_N}\ ; \tag{11}$$

here, $\gamma(=0.5772)$ is the Euler constant, and

$$\sigma_0=\sigma_1^{\tau_1}\sigma_2^{\tau_2}=125.8\ \text{MeV}/c\ , \tag{12}$$

so that

$$\gamma_L=\sqrt{1+\gamma_0^2 e^{-2\langle\ln\Theta\rangle}}\simeq\gamma_0 e^{-\langle\ln\Theta\rangle}\ , \tag{13}$$

with

$$\gamma_0=\frac{\sqrt{2}\sigma_0}{M_N}e^{-\gamma/2}=0.1422\ . \tag{14}$$

The mean value of $\ln\Theta$ is obtained experimentally by

$$\langle\ln\Theta\rangle=\frac{1}{n_f}\sum_{i=1}^{n_f}\ln\Theta_i\ , \tag{15}$$

where n_f is the number of fragments. Here, we must be careful of the contaminations of wounded protons and/or $\pi^\pm$'s in fragments, since their transverse momenta are, on average, approximately four times [24] larger than those produced in the evaporation process. To reduce such contribution, we omit minimum ionization track (relativistic protons and $\pi^\pm$'s) particles with the emission angle larger than five times the smallest emission angle, in addition to the cut made on the charge-sum restriction [see Eq. (A7) in Appendix A]. Thus, the number of fragments n_f we finally use is sometimes smaller than the number N_f including wounded protons.

There still remains some fear that the wounded protons and/or $\pi^\pm$'s might be counted in n_f. Therefore, we correct further for the contamination mentioned above with the use of the angular distribution of the fragment particles, details of which are presented in Appendix A.

The energy determination presented here is something like the modification of the well-known Castagnoli method [25], where we apply it for the fragment particles emitted from the projectile nucleus. The essential difference comes from the magnitude of the transverse momenta of secondaries.[1]

Now, let $E_{\text{est}}(=M_N\gamma_L-M_N)$ be the estimated energy of projectile presented above. In Fig. 7 we compare it with the true one E_{true} expected from the heavy-ion beam. One finds that the standard deviation σ is of the magnitude of 0.2–0.3 for $\log_{10}E_{\text{est}}/E_{\text{true}}$. The fluctuation of the energy thus estimated must be taken into account when calculating the absolute cosmic-ray intensity as presented later (see Sec. IV C).

C. Application to cosmic-ray data

In Table IV, we summarize the number of events for the measurement of emission angles of fragment particles with use of the microscope, after searching for the vertex point as described in Sec. II C (see Fig. 3). The numbers shown on the left-hand side are those measuring *completely* the emission angles for each fragment event detected by the autoscanning system. These data cover the cosmic-ray intensity in the low-energy region, from a few up to $\sim$100 GeV/N, and we use two units of

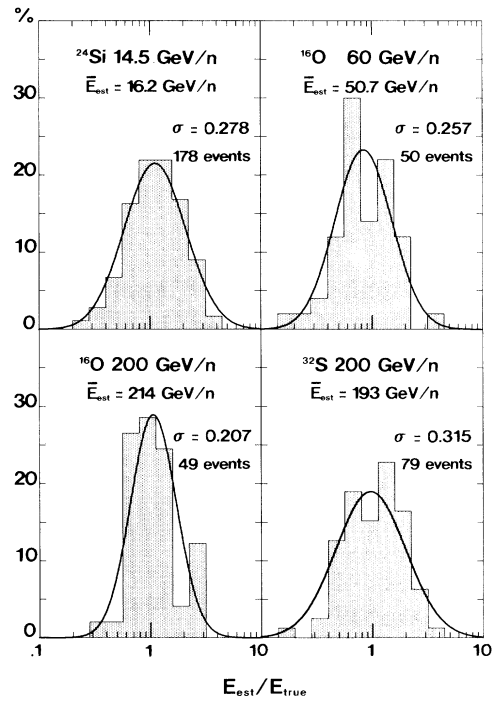

FIG. 7. Resolution of our energy determination calibrated by heavy-ion beams at several energies.

[1]The Castagnoli formula is derived from the well-known relation $\tan\theta\simeq\gamma_L\tan\theta^*/2$ between the laboratory system angle (θ) and the c.m. system (c.m.s.) angle (θ^*). This is obtained by the approximation $\epsilon^*=\sqrt{p^{*2}+m_\pi^2}\simeq p^*$ in c.m.s. This approximation is, however, not applicable in the case of evaporated fragments from nucleus. Instead, we have to use a relation $\epsilon^*=\sqrt{p^{*2}+M_N^2}\simeq M_N$ in the nucleus rest system, because of $p^*\simeq p_F\ll M_N$.

TABLE IV. Summary of event number performing emission-angle measurement of fragment particles with use of microscope. Left-hand numbers are those with no scanning bias, while the right-hand numbers are those with scanning-bias for high-energy events. Among ten units of chambers, two units (three in the case of sulfur) are used for the former, and eight (seven) units for the latter.

$Z_{min}-Z_{max}$	Non-biased measurement	Biased for high-energy event
13.5–14.5 (silicon)	696 (2 ch.)	491 (8 ch.)
15.5–16.5 (sulfur)	309 (3 ch.)	213 (7 ch.)
17.0–25.0 (sub-Fe)	972 (2 ch.)	781 (8 ch.)
25.0–40.0 (Fe-group)	533 (2 ch.)	480 (8 ch.)

chambers (three in the case of sulfur primary) for this purpose. For the remaining eight (seven) units, we have selected only high-energy fragment events with narrow angular spread in the microscope. Though the selection criterion for the "narrowness" is not unique, and varies slightly among different observers, we found no detection-loss bias for the energy larger than ~50 GeV/N as shown later.

We have determined the primary energy for individual elements using the method mentioned in the last subsection. To see the internal consistency of the energy determination, we checked first the reduced-angle distribution of α for various primaries as well as for various projectile energies.

We show the result in Fig. 8, where we plot an example of heavy-ion data [19] together and also draw the curve given by Eq. (9). We find that the shape of q^2 distribution for cosmic-ray data is remarkably similar to the heavy-ion data. Figure 9 shows q^2 distributions of several kinds of fragments (α, Li, Be, . . .) for various projectiles together with the fitting curve of Eq. (9). One again finds the same shape as in Fig. 6. These results indicate that the scaling nature holds for various kinds of projectiles and fragments as well as for a wide energy range from GeV/N to TeV/N. This evidence is also quite interesting in the study of high-energy nuclei interactions, but we leave this discussion for future publication.

Now we show the relative energy spectrum of primary iron in Fig. 10, where open circles indicate those obtained by the scanning with no detection-loss bias (two chambers), and the solid ones with scanning bias for high-energy events (ten chambers). One finds that the two spectra approach each other somewhere around 50 GeV/N, and we conclude that there is no detection-loss bias for the selection of high-energy events above 50 GeV/N. Practically, we combine these two spectra by using the open circles below 63.1 GeV/N, and the solid ones above it in this case. The continuation energy, 63.1 GeV/N, varies slightly in the different primary species (mostly around 50 GeV/N), and the experimental data on the absolute intensity and the abundance ratios presented in Sec. V are obtained by combining these two groups, nonbiased data (low-energy part) and the biased data (high-energy part), in this way.

The energy spectrum deviates downwards rapidly below 4 GeV/N, as shown in Fig. 10. This effect is due to the geomagnetic cutoff rigidity, and indicates that our energy determination was performed correctly. The curves

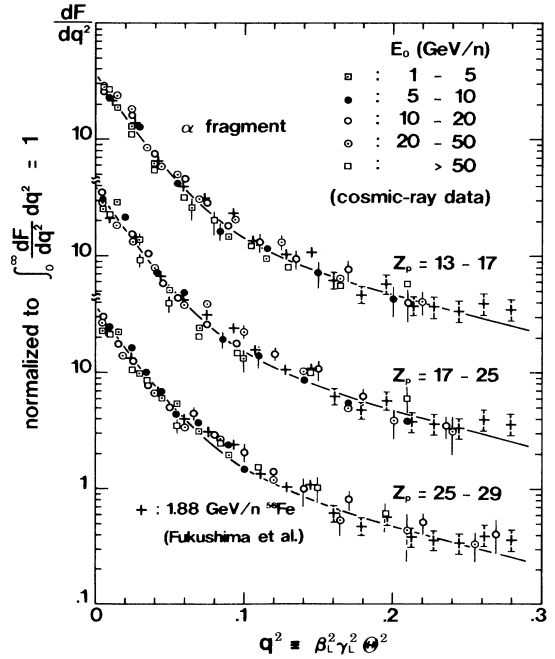

FIG. 8. q^2 distribution of α fragment obtained by the present cosmic-ray experiment for various projectiles as well as for several sets of energy range. Solid curve is the same as shown in Fig. 6.

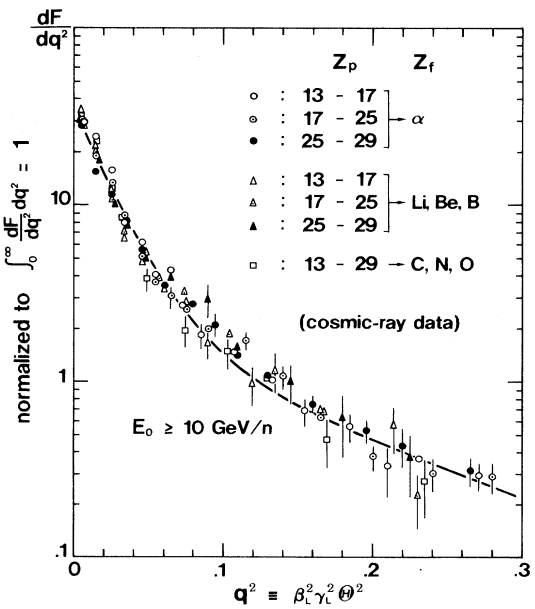

FIG. 9. q^2 distribution for various kinds of fragments, α~CNO, where we use only events with the projectile energy larger than 10 GeV/N. The solid curve is the same as in Fig. 6.

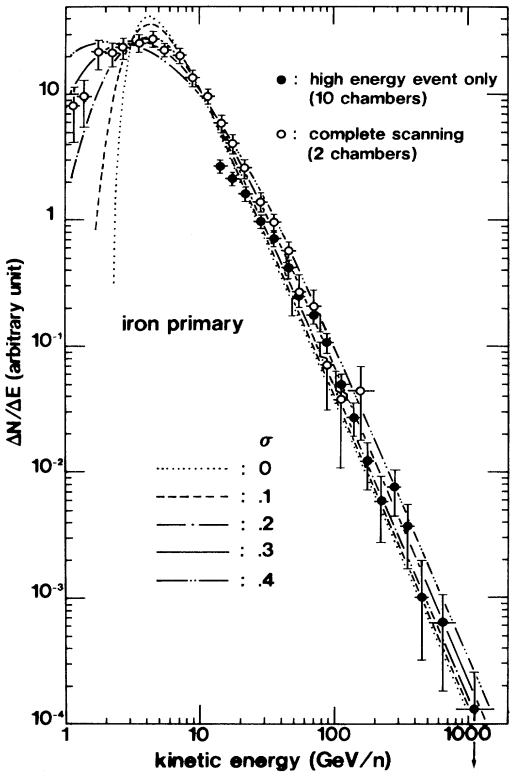

FIG. 10. Relative energy spectrum of iron component. Curves are obtained by the simulation calculation taking account of the geomagnetic cutoff momentum, including the effect of the energy resolution σ (see Sec. IV C).

drawn in Fig. 10 are obtained by simulation calculation taking into account both the effects of the limited energy resolution and of the cutoff rigidity, which are discussed in detail in Sec. IV C. One finds that the experimental data are in remarkable agreement with the calculation for $\sigma=0.2-0.3$, which are consistent with the values as shown in Fig. 7.

Here we should like to give some discussion on the applicability limit of our present energy determination method. Let us give some detailed accounts of our highest-energy event in connection with our method of energy determination. The event is named "Ev. 4301," and it is induced by a primary iron nucleus incident with zenith angle of 54.7°. The energy of the nucleus is determined to be 1.51 TeV/N.

The interaction point of this event is identified in an acrylic base of nuclear emulsion plate set at the third cycle in the jet detector (see Fig. 1), and the opening angles of the fragments are measured at the bottom nuclear emulsion plate. The relative distance l between these two emulsion plates is 6.21 cm, taking the zenith angle effect into account. So the geometrical spread r of the fragments at the bottom, for instance, in the case of protons, is of the magnitude

$$r=l\theta=l\frac{p_{TN}}{p_N}\simeq l\frac{\langle p_{TN}\rangle}{E_N}\simeq 6\ \mu\text{m}\ , \tag{16}$$

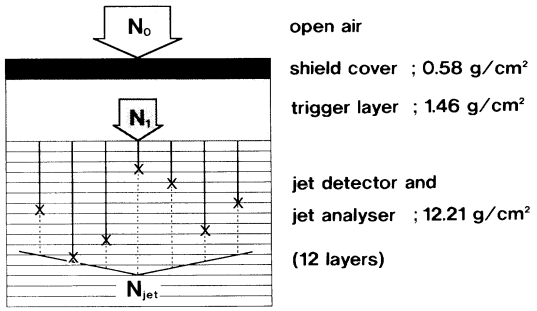

FIG. 11. Illustration of the cosmic-ray attenuation in the chamber for simulation calculation.

where the average of p_{TN} is assumed to be 146 MeV/c, from Eqs. (5) and (6). As the grain size of nuclear emulsion used here (Fuji ET7B-type) is, on average, $\sim 0.6\ \mu$m diam, the tracks of the fragments concerned are well resolved in the microscope. In Appendix A, we demonstrate typical examples of (reduced) angular distribution of fragments, including the event of the highest energy mentioned above.

Of course, one should be reminded it was rather lucky that the interaction of the Ev. 4301 occurred at the upper layer in the jet detector. If the interaction point were at the lower layer near the bottom, the measurement of the opening angle would be quite hard. In order to eliminate such difficulty, we omit the fragment events occurred in the last two cycles, that is, we use only those found in the upper 12 cycles of the jet detector (see Figs. 1 and 11). Fortunately in this observation, we faced none of the fragment events with track confusion.

The upper limit of measurable energy in the present chamber design would be ~ 5 TeV/N although it would depend on the interaction position and on the incident zenith angle. If, further, we were allowed to have two orders of magnitude larger exposures which would bring us ~ 100 TeV/N heavy primaries, then we would need ~ 1-m-thick spacers in order to make practicable the opening-angle measurement.

IV. CONVERSION TO ABSOLUTE INTENSITY OF PRIMARY

A. Detection efficiency

Often it is not very straightforward to calculate the detection efficiency for a counter experiment because of somewhat complicated geometry. In our opinion it constitutes at least one reason why the proton-satellite [2] data for the proton component is so questionable. In our case, the calculation is very easy because the chamber geometry is rather simple (see Fig. 1), and the only problem is in the cross section for the nucleus-nucleus collisions. We consider two typical cross-section models, the hard-sphere model by Hagen *et al.* [26] and the soft-sphere model by Karol [27].

The explicit form for the former cross section is given by

$$\sigma_R = \pi r_0^2 (A_P^{1/3} + A_T^{1/3} - \zeta)^2 , \quad (17)$$

where A_P (or A_T) is the mass number of the projectile (or target) nucleus, respectively, and

$$r_0 = 1.29 \times 10^{-13} \text{ cm}$$

and (18)

$$\zeta = 1.189 \exp[-0.054\,46 \min(A_P, A_T)] .$$

On the other hand, Karol derived the following formula which includes the energy dependence of the nucleon-nucleon cross section:

$$\sigma_R = \pi(a_P^2 + a_T^2)[\ln\chi + \mathrm{Ei}(\chi) + \gamma]$$
$$\text{with } \chi = \sigma_{NN} A_P A_T / \pi(a_P^2 + a_T^2) , \quad (19)$$

where γ is the Euler constant (=0.5772), Ei is the exponential integral function, and σ_{NN} is the energy-dependent cross section for the nucleon-nucleon interaction, and a_P (or a_T) is related to the nuclear root-mean-square radius of the projectile (or target) nucleus (see Ref. [27] for detail).

In Table V, we summarize the collision mean free paths in the case of four typical projectiles (O, Si, Ca, and Fe) for several kinds of target materials relevant to the present chamber, as well as for the air target which is neessary in the next subsection. Here the unit is g/cm^2 and the numerical values without a specification for the projectile energy E_0 ("–") are obtained from Eq. (17), while those corresponding to 10 and 1000 GeV/N are calculated from Eq. (19).

One finds that the effect of the energy dependence of the cross section is at most a few percent in the energy range of GeV/N to TeV/N and also that the difference between the two models is not significant in our energy range. Both effects are negligible in comparison with the experimental (and statistical) errors. In the present work, we use the cross section at $E_0 = 20$ GeV/N from Eq. (19).

Now we need the observed number of heavy primaries *at chamber top* (including methacrylic light-shield box as well as the wood cover). We performed a simulation calculation taking into account the detailed structure as demonstrated in Fig. 11. We assume that N_0 is the total number of projectiles at the chamber top, N_1 is the number of projectile passing through the trigger layer, and N_{jet} is the number interacting inside the jet-detector section, where the latter two N_1 and N_{jet} are observable in our experiment.

The zenith angle of projectile at the chamber top is sampled according to the integrand of Eq. (B2) in Appendix B, and we follow the projectile until it either leaves the chamber or collides with chamber material. We omit fragment events occurring within 3 mm from the edge of the nuclear emulsion plate because it is often difficult to measure the emission angle of the fragments near the edge.

In Table VI, we summarize the numerical results of $\kappa = N_{\text{jet}}/N_0$ we need here, as well as those of $\kappa' = N_{\text{jet}}/N_1$. Since the latter is observable in our chamber, we also show experimental data ($=\kappa'_{\text{obs}}$) in the table, and find they agree quite well with each other.

TABLE V. Numerical values of collision mean free paths for four typical projectile nuclei in several materials relevant to our chamber. The unit is g/cm^2.

Target nucleus Density (g/cm^3)	E_0(GeV/N)	Projectile nucleus O (g/cm^2)	Si (g/cm^2)	Ca (g/cm^2)	Fe (g/cm^2)
Methacryl	–	18.7	14.3	12.0	10.1
$\rho = 1.21$	10	19.9	14.8	11.7	10.0
	1000	19.5	14.5	11.6	9.9
Emulsion	–	44.4	34.8	29.7	25.7
$\rho = 3.73$	10	46.5	36.5	30.4	26.7
	1000	45.8	36.1	30.1	26.4
Gd_2O_2S:Tb	–	66.9	54.1	47.6	42.3
$\rho = 7.34$	10	70.8	58.2	50.5	45.6
	1000	70.8	57.7	50.1	45.1
Stainless steel	–	51.7	40.4	34.9	30.6
$\rho = 7.91$	10	52.2	42.7	37.0	33.2
	1000	51.7	42.3	36.7	32.9
Air	–	23.7	19.0	16.3	14.1
	10	25.3	19.5	16.2	14.2
	1000	24.9	19.3	16.0	14.0

TABLE VI. Simulated results for $\kappa=N_{\rm jet}/N_0$ and $\kappa'=N_{\rm jet}/N_1$, and the observed ones $\kappa'_{\rm obs}$ for several primaries.

Primary / κ	Si	S	A	Ca	Ti	Cr	Fe
$\kappa=N_{\rm jet}/N_0$	0.265	0.278	0.275	0.282	0.284	0.277	0.281
$\kappa'=N_{\rm jet}/N_1$	0.310	0.328	0.330	0.339	0.345	0.339	0.346
$\kappa'_{\rm obs}$	0.322	0.326	0.339	0.332	0.332	0.335	0.324

This means that the cross section expressed by Eq. (19) nicely reproduces the experimental data in the region of GeV/N to TeV/N. The number $N_{\rm jet}^{\rm (obs)}(Z_0;Z_{\rm min},Z_{\rm max})$ actually observed in the jet detector is not equal to $N_{\rm jet}$ mentioned above, but we have to take the effect of charge resolution into account as discussed in Sec. II C:

$$N_{\rm jet}^{\rm (obs)}=\nu N_{\rm jet}=\nu\kappa N_0 \ ; \tag{20}$$

i.e., dividing the observed number within the charge range $Z_{\rm min}\sim Z_{\rm max}$ by $\nu\kappa$, we can get the total number of projectiles with charge Z_0 at the chamber top.

B. Fragmentation process of primary in air

Since our observation level is ~ 10 g/cm^2, we have to carefully take into account the effect of the fragmentation in the atmosphere in order to get the absolute intensity of primaries at top of the atmosphere. Let $I_i^{(0)}$ be the absolute intensity of nucleus i at top of the atmosphere. Throughout this subsection, we omit the energy term in the intensity because, as seen in the last subsection, both the interaction mean free path (mfp) and the fragmentation parameter are nearly energy independent in the energy range of interest.

Since the effective solid angle at top of the atmosphere is given by

$$\Omega_0=\int\int_{\Omega\le 2\pi}\cos\theta\, d\Omega=\pi \ , \tag{21}$$

the total number of nuclei of type i coming into the chamber at the top of the atmosphere is given by

$$N_i^{(0)}=S\Omega_0 T I_i^{(0)}=\pi S T I_i^{(0)} \ , \tag{22}$$

where S is the chamber area and T is the duration time of the balloon.

Let $N_{i\to j}$ be the number of nuclei of type j at observation level t (chamber top) coming from the fragment process of the primary i (total number at top of the atmosphere$=N_i^{(0)}$) during the passage in air ($i\to j$, $i\to l\to j, i\to l\to m\to j, \ldots$). Now we introduce a parameter η_{ij} to relate these two:

$$N_{i\to j}(t)=\eta_{ij}(t)N_i^{(0)}e^{-t/\lambda_i} \ , \tag{23}$$

where λ_i is the collision mfp of primary i in the atmosphere. The parameter η_{ij} is related to the fragmentation parameter $P_{ij},\lambda_i,\lambda_j$ and also to the observation level t. We present its explicit form in Appendix B for the simple case so as to understand its physical meaning. Here we neglect the energy dependence of λ_i as discussed in the last subsection.

Now, on the basis of a large amount of data ($\sim$6000 events) on fragmentation of various primaries occurring in our chamber, we can make a sampling generator for P_{ij}. In Fig. 12, we present three examples of a sampling-generator curve in the cases of $i=$Si, Ca, and Fe for air-like targets. In Figs. 13(a) and 13(b), we demonstrate the experimental data on P_{ij} in the cases of $i=$Si and Fe as well as the sampling-generator curve, where we plot also the data obtained by Freier and Waddington [28] (air target), heavy-ion beam [29–31] (carbon target), and the numerical data by Tsao and Silberberg [32] (air target). Although Silberberg's numerical data give somewhat smaller values than experimental ones, the others are in agreement with each other. Our open circle data, which appears in Fig. 13 corresponding to the fragmentation probability with small charge transition $\Delta Z=0\sim 1$, are obtained from the analysis of the attenuation of heavy primaries in the atmosphere, details of which are presented in Appendix C.

These data also bring us quite important information for the study of high-energy nucleus-nucleus interactions and, in fact, we found some regularity in the nuclear spallation-fragmentation process [33]. We do not go deep into these results here, but we will report the details elsewhere since it deviates slightly from the emphasis of this article.

We have to perform a simulation calculation to get more practical values of η_{ij} than those shown in Appendix B, since the latter is somewhat simplified. In Table VII, we explicitly give the numerical values of η_{ij} for even nuclei with i(and/or j)$=$Fe to Si, obtained by the simulation calculation.

From Eqs. (20), (22), and (23), the observed number of nuclei of type j found in the jet detector is given by

$$N_j^{\rm (obs)}=\nu_j\kappa_j\sum_{i\ge j}N_{i\to j}=\pi S T\nu_j\kappa_j\sum_{i\ge j}\eta_{ij}I_i^{(0)}e^{-t/\lambda_i} \ . \tag{24}$$

Defining the intensity

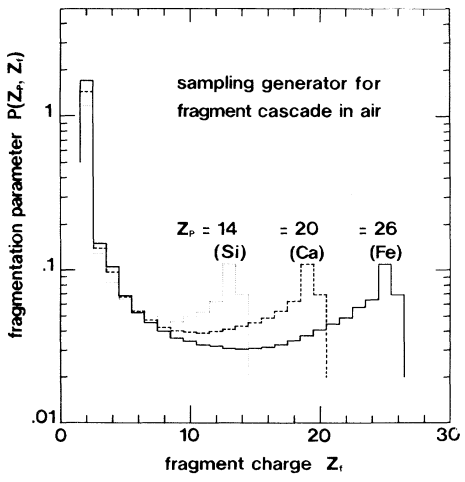

FIG. 12. Examples of sampling curves for fragmentation parameter.

TABLE VII. Numerical values of η_{ij} obtained by the simulation calculation, where i denotes the primary and j its fragment.

j \ i	Fe	Cr	Ti	Ca	A	S	Si
Fe	0.6774	0	0	0	0	0	0
Cr	0.0473	0.6722	0	0	0	0	0
Ti	0.0362	0.0462	0.6809	0	0	0	0
Ca	0.0319	0.0380	0.0465	0.6914	0	0	0
A	0.0251	0.0325	0.0332	0.0454	0.7240	0	0
S	0.0268	0.0259	0.0337	0.0357	0.0490	0.7298	0
Si	0.0237	0.0276	0.0257	0.0275	0.0321	0.0438	0.7547

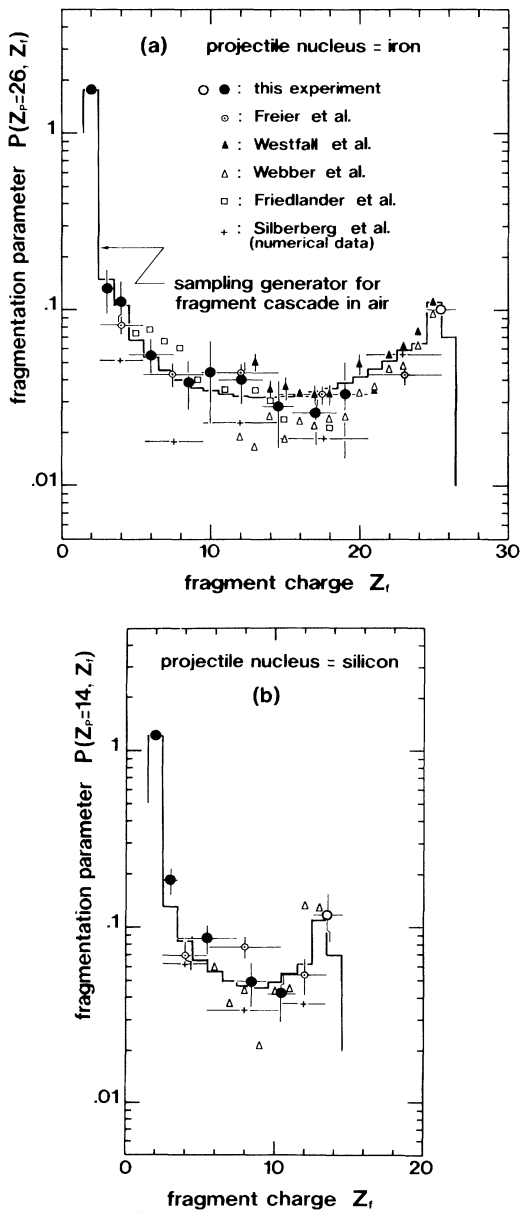

FIG. 13. Fragmentation parameter obtained by this work and the others in the cases of (a) iron and (b) silicon projectiles against airlike target.

$$I_j^{(\mathrm{obs})}=N_j^{(\mathrm{obs})}/\pi ST$$

$$\text{with } \pi ST=3.827\times10^5 \text{ m}^2\,\text{s}\,\text{sr} , \quad (25)$$

we obtain the absolute intensity $I_i^{(0)}$ of primary $i(=\mathrm{Si}, \mathrm{P}, \mathrm{S}, \ldots, \mathrm{Fe})$ at the top of the atmosphere by solving the following equations simultaneously:

$$\mathbf{H}\cdot\mathbf{I}^{(0)}=\mathbf{I}^{(\mathrm{obs})} , \quad (26)$$

where

$$H_{ij}=(\nu_j\kappa_j\eta_{ij}e^{-t/\lambda_i}) \text{ with } H_{ij}=0 \text{ for } i<j . \quad (27)$$

The explicit numerical values of H_{ij} are obtained from the data shown in Tables III and V–VII, and Eq. (26) can be solved by the use of a Gauss-Jordan method. The solution of Eq. (26) is summarized in Sec. V A (see Table VIII) for several typical elements after correcting for the effects of geomagnetic cutoff momentum and the energy resolution as discussed in the next subsection.

The above procedure eliminates the contamination of the *fragment* particle j (coming from heavier primaries $i=j+1, j+2, \ldots$) for the absolute intensity of the *primary* particle j we need. Nevertheless, one may still comment that the experimental uncertainty ΔP_{ij} inherent in the fragmentation parameter P_{ij} will bring us some trouble in determining the absolute intensity.

In Appendix D, we explicitly present the contamination rate of *secondary* fragments for the *primary* element we need, and also discuss the effect of the uncertainty ΔP_{ij} for the absolute intensities. We show that it is negligible for silicon and sulfur elements and allowable enough for calcium. This is because the most effective components are diagonal ones ($i=j$), one order of magnitude larger than the others, as seen in Table VII. That is, the diagonal ones depend mainly on the attenuation length only (see also Appendix C), while the off-diagonal cases depend on the fragmentation parameters. For the relatively rare elements, however, such as argon and titanium, one should expect an uncertainty of as large as 15–25 % in the absolute intensity, originated mainly in the uncertainty of the fragmentation parameter ΔP_{ij} (see Appendix D).

TABLE VIII. Absolute intensities of typical heavy elements obtained by the present work, where the intensity is multiplied by $E_0^{2.5}$ (E_0 is the primary energy in GeV per nucleon), and ± denotes the statistical error. The numerical values with parentheses are the number of events to obtain the absolute fluxes. The mean energy for each energy bin (E_{min},E_{max}), is calculated by $\sqrt{E_{min}E_{max}}$.

E_0 (GeV/N) Energy range	$E_0^{2.5}\Delta I/\Delta E_0$ [$m^{-2}s^{-2}sr^{-2}(GeV/N)^{1.5}$] Silicon	Sulfur	Calcium	Iron	$Z=17-20$	$Z=21-25$
3.98–5.01	0.90±0.14 (40)	0.168±0.400 (18)	0.155±0.036 (18)	1.11±0.15 (56)	0.375±0.065 (33)	0.302±0.050 (36)
5.01–6.31	1.15±0.16 (50)	0.175±0.041 (18)		1.20±0.16 (58)	0.453±0.072 (40)	0.308±0.051 (37)
6.31–7.94	1.24±0.17 (50)	0.248±0.051 (24)	0.110±0.033 (11)	1.45±0.18 (66)	0.407±0.071 (33)	0.437±0.063 (48)
7.94–10.0	1.89±0.22 (72)	0.234±0.052 (20)		1.42±0.19 (57)	0.510±0.083 (38)	0.525±0.072 (53)
1.00–1.26(×10)	1.80±0.24 (58)	0.364±0.070 (27)	0.208±0.052 (16)	1.35±0.20 (47)	0.381±0.076 (25)	0.495±0.075 (44)
1.26–1.59	2.04±0.27 (55)	0.304±0.072 (18)		1.37±0.22 (38)	0.527±0.098 (29)	0.488±0.061 (64)
1.59–2.00	2.12±0.30 (49)	0.396±0.091 (19)	0.212±0.092 (6)	1.51±0.26 (34)	0.542±0.111 (24)	
2.00–2.51	2.01±0.33 (36)	0.428±0.106 (16)	0.178±0.040 (20)	1.54±0.30 (27)	0.598±0.130 (21)	0.299±0.092 (19)
2.51–3.16	2.14±0.39 (30)	0.381±0.076 (25)	0.140±0.040 (12)	1.26±0.32 (18)	0.745±0.166 (20)	0.385±0.103 (14)
3.16–3.98	1.76±0.22 (66)	0.386±0.074 (27)	0.201±0.056 (13)	1.62±0.41 (16)	0.641±0.178 (13)	0.414±0.055 (57)
3.98–5.01	1.42±0.22 (41)	0.354±0.084 (18)	0.187±0.062 (9)	1.68±0.48 (12)	0.425±0.075 (32)	0.391±0.062 (40)
5.01–6.31	1.72±0.27 (41)	0.437±0.109 (16)	0.169±0.069 (6)	1.36±0.51 (7)	0.396±0.084 (22)	0.292±0.062 (22)
6.31–7.94	1.66±0.27 (39)	0.452±0.130 (12)	0.271±0.100 (7)	1.55±0.29 (29)	0.420±0.102 (17)	0.328±0.077 (18)
7.94–10.0	1.38±0.28 (24)	0.423±0.150 (8)	0.213±0.106 (4)	1.65±0.35 (22)	0.441±0.122 (13)	0.291±0.065 (20)
1.00–1.26(×10^2)	1.20±0.30 (15)	0.396±0.132 (9)	0.129±0.074 (3)	1.38±0.38 (13)	0.357±0.099 (13)	
1.26–1.59	1.40±0.39 (13)			1.34±0.45 (9)		0.289±0.118 (6)
1.59–2.00	1.04±0.39 (7)	0.296±0.209 (2)		1.05±0.47 (5)	0.214±0.107 (4)	0.202±0.117 (3)
2.00–2.51	0.59±0.26 (5)	0.352±0.203 (3)		1.37±0.48 (8)		0.222±0.111 (4)
2.51–3.16						
3.16–3.98	0.70±0.40 (3)	0.386±0.273 (2)	0.051±0.051 (1)	1.22±0.61 (4)	0.247±0.143 (3)	0.218±0.154 (2)
3.98–5.01						
5.01–6.31	0.36±0.36 (1)			1.39±0.98 (2)	0.221±0.221 (1)	0.163±0.163 (1)
6.31–7.94						
7.94–10.0				1.09±1.09 (1)		0.191±0.191 (1)
1.00–1.26(×10^3)						
1.26–1.59						

C. Effects of energy resolution and geomagnetic cutoff momentum

In the last subsection we obtained the absolute primary intensity at the top of the atmosphere from our observational data. Other important effects for the absolute primary intensity are those coming from the energy resolution and the geomagnetic cutoff momentum as discussed in Sec. III C. The first effect can easily be estimated in the following way.

Let E be the estimated energy and E_0 the true energy. Then, from the consideration in Sec. III B, the distribution function of E is expressed as

$$f(E_0,E)dE=e^{-y^2/2\sigma^2}\frac{dy}{\sqrt{2\pi}\sigma} \quad \text{with } y=\log_{10}\frac{E}{E_0} . \tag{28}$$

Here σ is of the magnitude 0.2–0.3 as expected from the calibration with use of the heavy-ion beam (see Fig. 7 in Sec. III B). Let $dI^{(0)}_{\rm est}(E)/dE$ be the differential absolute intensity obtained by the procedure mentioned in the last subsection, and $dI^{(0)}_{\rm true}(E_0)/dE_0$ be the true one. Then we have a relation

$$\frac{dI^{(0)}_{\rm est}}{dE}=\int_0^\infty \frac{dI^{(0)}_{\rm true}}{dE_0}f(E_0,E)dE_0 . \tag{29}$$

Since the shape of the spectrum is nearly powerlike in the energy region $E_0 \gtrsim 20$ GeV/N (see Fig. 10), we can assume

$$I^{(0)}_{\rm true}(E_0)=I_0E_0^{-\beta} . \tag{30}$$

In this case, Eq. (29) is simply written as

$$\frac{dI^{(0)}_{\rm est}}{dE}=\beta I_0E^{-\beta-1}e^{\delta^2}=e^{\delta^2}\frac{dI^{(0)}_{\rm true}}{dE} , \tag{31}$$

i.e.,

$$\frac{dI^{(0)}_{\rm true}}{dE}=e^{-\delta^2}\frac{dI^{(0)}_{\rm est}}{dE} \quad \text{with } \delta=\frac{\ln 10}{\sqrt{2}}\beta\sigma , \tag{32}$$

that is, we must reduce the observed flux by $e^{-\delta^2}$ in this case, taking the fluctuation of the energy determination into account. For instance, setting $\beta\simeq 1.5$ and $\sigma\simeq 0.25$, we must reduce the observed flux by 31%.

Since the above consideration is applicable only for the high-energy region $\gtrsim 20$ GeV/N, we have to perform a simulation calculation, taking into account the geomagnetic cutoff momentum, effective around a few ~ 10 GeV/N as follows.

Though Inoue, Wada, and Kondo [34] have reported the calculation of the geomagnetic cutoff momentum at Sanriku latitude with $[N,E]=[39.16°,141.83°]$, we have performed more practical calculations along the line of the present experiment, details of which are presented in Appendix E.

We have stored on hard disk all the data of the geomagnetic cutoff momentum, $R_{\rm cut}(\theta,\phi)$ for various zenith and azimuthal angles (step width; $\Delta\theta=2°$ and $\Delta\phi=1°$), and performed a simulation calculation including the fluctuation of the energy determination mentioned before. Here we assume the exponent of the primary spectrum is 1.5 (integral) for iron and 2.0 for silicon so as to be consistent with our experiment in the energy region $\gtrsim 20$ GeV/N, and we use the primary spectrum shape consistent with HEAO-3 data [6] in the lower-energy region $\lesssim 10$ GeV/N.

In Fig. 10 (Sec. III C), we demonstrate the numerical results for several choices of the energy resolution σ together with the experimental data. Naturally, the spectrum drops rapidly around $\lesssim 3$ GeV/N in the case of $\sigma=0$, due to the geometrical cutoff momentum. One finds that the experimental data is in agreement with the numerical results for $\sigma=0.25$–0.30, nicely consistent with the analysis of the heavy-ion beam data (see Fig. 7). From this, we believe our energy determination is performed satisfactorily.

We find that both the energy resolution and the geomagnetic cutoff momentum contribute significantly to the observed intensity. Now, let $C_R(E)$ be the ratio of the intensity neglecting such effects to that including them. We show in Fig. 14 the numerical results for several cases of σ obtained by simulation calculation.

Finally we get the true intensity of primary

$$\frac{dI^{(0)}_{\rm true}}{dE}=\frac{1}{C_R(E)}\frac{dI^{(0)}_{\rm est}}{dE} . \tag{33}$$

One finds that the numerical value shown in Fig. 14 is surely in accord with the analytic one ($=e^{\delta^2}$) in Eq. (32) at higher energy. For sub-Fe group, we set $\beta=1.7$ to calculate the correction parameter $C_R(E)$.

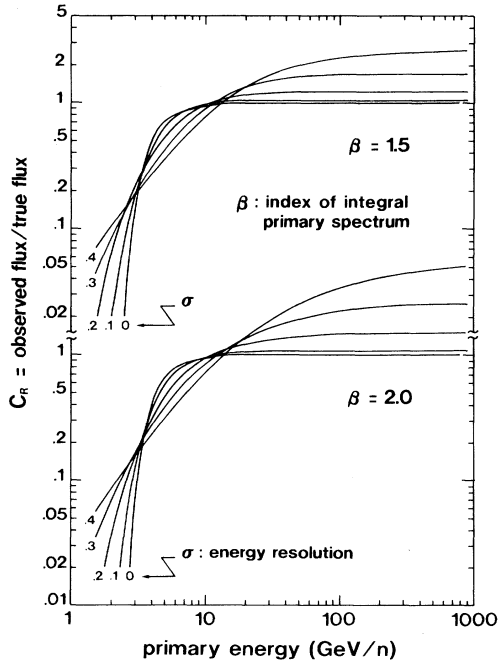

FIG. 14. Numerical value of C_R, the correction parameter for cutoff momentum, as a function of the primary energy, in the case of $\beta=1.5$ and 2.0. σ attached to curves denotes the resolution of the energy determination appeared in Fig. 7.

V. RESULTS AND DISCUSSIONS

A. Absolute intensity of primary

Let us summarize in Table VIII the absolute intensities (multiplied by $E_0^{2.5}$) at the top of the atmosphere for several typical elements obtained by the procedure mentioned in the last section, where we give the number of events together in each energy bin with parentheses. In the low-energy region $\lesssim 10$ GeV/N, we have some detection-loss bias in the case of lighter elements such as silicon and sulfur, because we sometimes miss a nuclear interaction event with small multiplicity and with large opening angle, unless the vertex point is identified in a nuclear emulsion plate.

In Fig. 15, we present the absolute intensities of various primaries against the primary energy per nucleon obtained by the present work, where the vertical axis is multiplied by $E_0^{2.5}$ to emphasize the spectral features. One finds that the slope of the silicon spectrum becomes steeper at energy $\gtrsim 50$ GeV/N, while that of iron is almost flat in the wide energy range from 10 GeV/N – 1000 GeV/N and beyond. The strong point of our data is in covering the wide energy range from a few GeV/N to a few TeV/N with use of a *single detector* and a *unified method* for both the energy and the charge determination, so that the relative spectrum and its slope index are highly reliable, as long as the scaling nature holds in the angular distribution of nuclear fragments after a spallation reaction.

A result similar to ours on the silicon spectrum was first reported by the Spacelab-2 experiment [7]. We compare our data on the intensities of silicon and iron with several others [6,7,35] in Figs. 16(a) and 16(b), respectively. It is remarkable that both the Spacelab-2 and our data on Si spectrum show a steep exponent in the higher-energy region, while all groups give consistent results on the Fe spectrum, both in the shape (flat spectrum) and the absolute value, though Simon *et al.* [35] give a slightly higher flux.

The steep slope of the Si-spectrum is quite hard to understand in the framework of the current models for interstellar propagation, and it may bring us some new problem for high-energy particle astrophysics. We should be, however, more cautious in interpreting the spectrum-index problem, either softer or harder, and not jump to a conclusion without considering the possibility of a statistical fluctuation, an overestimation of chamber efficiency, etc. In any event, we should investigate this result through further observational cross checks.

B. Abundance ratio of sub-Fe/Fe

It is known that the abundance ratios of B/C and/or sub-Fe/Fe bring valuable information on the estimation of the escape length λ_e of cosmic rays in the Galaxy. In our observation, while it is difficult to detect boron to carbon without detection-loss bias, we have fruitful data on sub-Fe/Fe.

In Figs. 17(a)–17(c), we present the abundance ratios of sulfur, argon, and calcium to the Fe group (≡Fe+Co+Ni in our data) against the primary energy, where we plot the other data together [7,36]. Our data

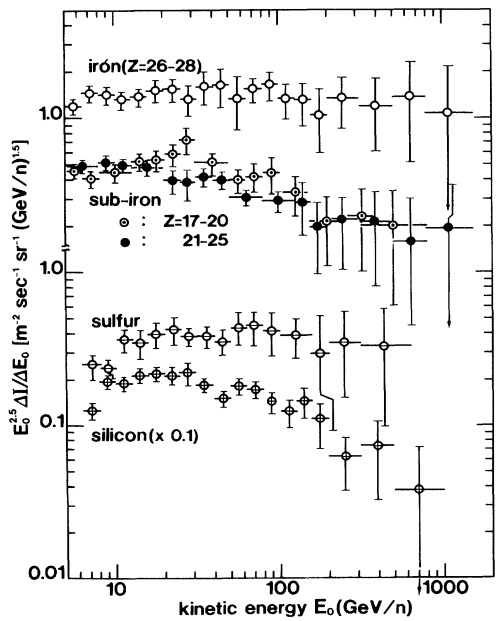

FIG. 15. Absolute differential intensities for several primary elements obtained by the present work, where the vertical axis is multiplied by $E_0^{2.5}$ to emphasize the spectral feature.

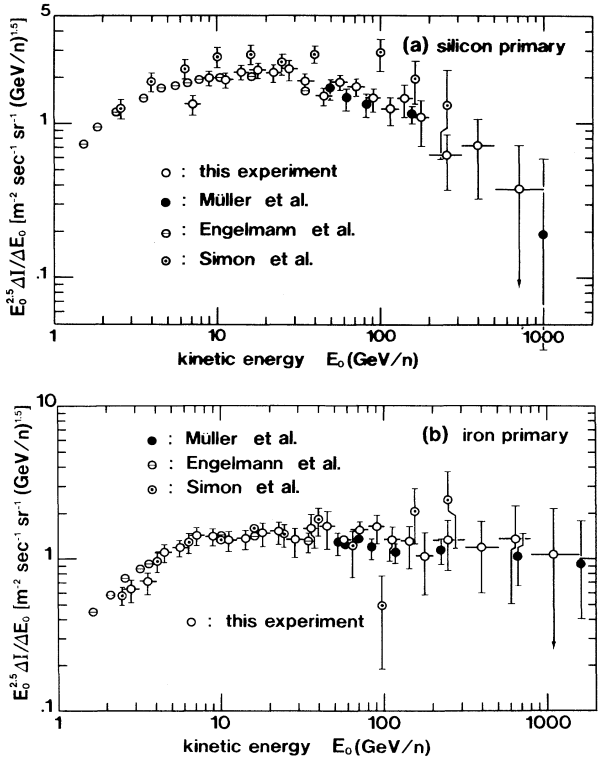

FIG. 16. Absolute differential intensities of (a) silicon and (b) iron, together with those obtained by typical other observers.

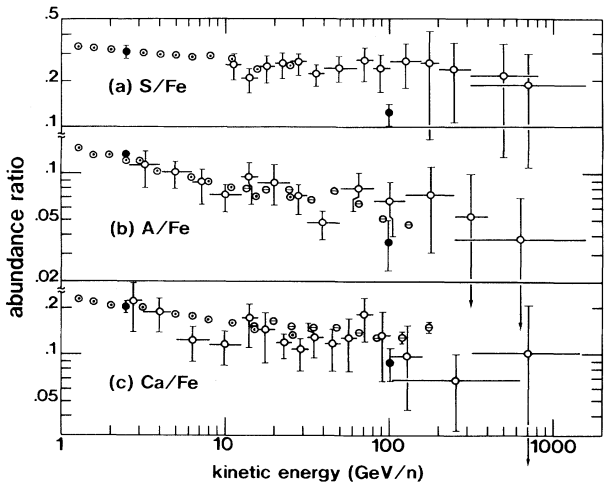

FIG. 17. Abundances of (a) sulfur, (b) argon, and (c) calcium, relative to iron ($26 \leq Z \leq 28$) as a function of primary energy per nucleon. ○: this work; ●: Müller *et al.*; ⊙: Engelmann *et al.*; ⊖: Binns *et al.*

suggests that all ratios decrease in the form of power laws from GeV/N to TeV/N, while the Spacelab-2 data [7] gives somewhat lower values at ~ 100 GeV/N, nearly comparable with those at the source.

In Figs. 18(a) and 18(b), we show the abundance ratios of two types of sub-Fe, (a) $Z=21-25$ and (b) $Z=17-25$, to the Fe group together with those obtained by other groups [36]. In the cases of Figs. 17(a)–17(c), we have some problems about the purity of each element (see Table III), while in the case of Figs. 18(a) and 18(b), such a problem is much reduced. Again we find they decrease in the form of power laws over a wide energy range, from 500 MeV/N to 1000 GeV/N and beyond. Although one may remember that our data in Figs. 17(b) and 18 include the uncertainty of 15–25 %, coming mainly from the uncertainty of the fragmentation parameter ΔP_{ij}, as discussed in the end of Sec. IV B (also in Appendix D), it is still well within statistical fluctuations.

Preliminary analysis [10,13] indicates that the abundance ratios presented here are all well reproduced by the "leaky box model" with $\lambda_e \propto R^{-0.5}$ to $R^{-0.6}$ from a few GeV/N up to a few TeV/N, for the source spectrum proportional to $R^{-2.2}$ irrespective of the species, though including the uncertainty in the choice of the source abundances. Results of the full analysis will be reported elsewhere in the near future.

C. All-particle spectrum

In order to get the all-particle spectrum, we have to sum up individual primary elements from proton to iron. In Figs. 19 and 20, we show individual primary spectra in GeV/particle obtained by our present and previous works together with those by others [37–39], where our data on proton and helium refer to the 1987 experiment [4]. It is, however, not so straightforward to superpose these for individual energy bins, since the procedures of the data analyses are not always the same among observers, varying individually in the error estimations (both statistical and experimental), in the detection-loss bias (particularly in the lower-energy region in the case of emulsion chamber experiments), and in bin width of the particle energy. In the present work, we interpolate the experimental data by fitting straight lines for proton and helium, and by drawing curves for heavy elements to guide the eye.

In Fig. 19, we show solid straight lines determined by the least sum of the squares method, assuming powerlike spectra for proton and helium. They are expressed as

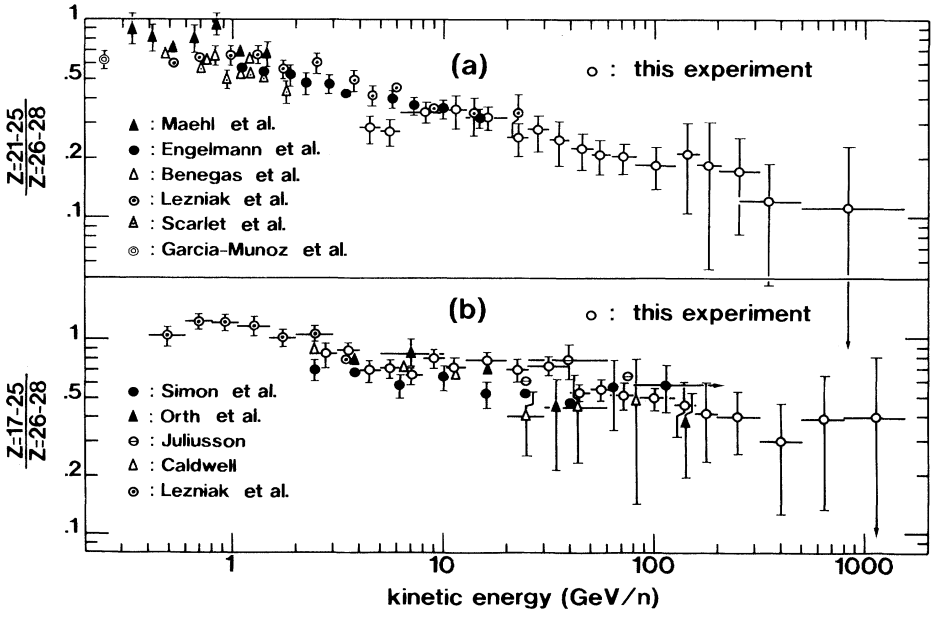

FIG. 18. Abundances of sub-Fe groups, (a) $Z=21-25$ and (b) $Z=17-25$, relative to iron as a function of primary energy per nucleon.

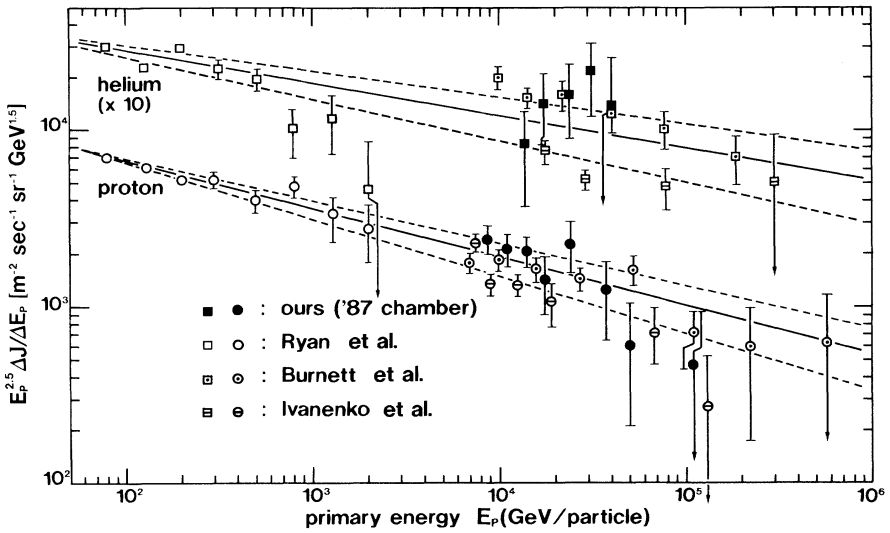

FIG. 19. Fluxes of proton and helium components as a function of energy per particle.

$$\left[\frac{dJ}{dE_P}\right]_p = 2.43\times10^4 \left[\frac{E_P}{\text{GeV/particle}}\right]^{-2.78\pm0.04}, \tag{34a}$$

$$\left[\frac{dJ}{dE_P}\right]_{\text{He}} = 6.31\times10^3 \left[\frac{E_P}{\text{GeV/particle}}\right]^{-2.68\pm0.05}, \tag{34b}$$

in unit of flux $m^{-2}\,s^{-1}\,sr^{-1}$ (GeV/particle)$^{-1}$.

Since the experimental data of both proton and helium components fluctuate considerably in the higher-energy region $\gtrsim 10$ TeV/particle, we draw two broken straight lines together, denoting the upper fit to JACEE [37] and ours [4], and the lower to the satellite data recently obtained by the group at Moscow State University [38].

Though the JACEE group [37] points out that their helium flux exceeds significantly the expected one extrapolated from the lower-energy data by Ryan, Ormes, and Balasubrahmanyan [39], we regard the rapid drop appearing in the region of 1–3 TeV/particle as a statistical fluctuation. Of course, we should confirm it further in the region of 1–10 TeV/particle.

For the heavier components shown in Figs. 20(a) and 20(b), we interpolate by eye the individual experimental points of different groups [6,7,35–37]. One may worry that such interpolation of the experimental points by eye

TABLE IX. Interpolated flux values, $E_P^{2.5}\Delta J/\Delta E_P$ ($m^{-2}\,s^{-1}\,sr^{-1}\,GeV^{1.5}$), at several energies for individual primary elements. Parentheses denote the value obtained by the extrapolation of guiding curve shown in Figs. 20(a) and 20(b), and ± found in proton and helium elements does not mean the statistical error, but the upper and lower values corresponding to the broken lines shown in Fig. 19.

Primary \ E_P (GeV)	10^2	2×10^2	5×10^2	10^3	2×10^3	5×10^3	10^4	2×10^4	5×10^4	10^5	2×10^5	5×10^5
Proton	6690 ±30	5510 ±200	4260 ±300	3510 ±340	2900 ±370	2240 ±350	1840 ±340	1520 ±330	1170 ±290	970 ±290	800 ±260	620 ±225
Helium	2750 ±200	2430 ±230	2060 ±300	1820 ±300	1610 ±300	1360 ±310	1200 ±290	1060 ±290	900 ±290	790 ±280	700 ±270	(595) ±250
Carbon	440	440	400	350	300	235	190	155	(119)	(96)	(79)	(60)
Nitrogen	180	175	140	110	86	60	45	34	(24)	(17)	(14)	(9)
Oxygen	650	710	680	630	555	455	385	320	(245)	(202)	(166)	(129)
Neon	160	173	160	140	118	91	75	61	(46)	(38)	(31)	(23)
Magnesium	250	285	284	263	240	205	180	153	(125)	(108)	(92)	(75)
Silicon	235	280	300	284	230	148	93	55	(25)	(14)	(8)	(3)
Sulfur	36	52	71	78	75	65	55	(44)	(30)	(22)	(15)	(9)
Sub-Fe	124	214	307	302	270	205	156	114	73	(48)	(33)	(20)
Fe group	195	420	580	620	630	610	570	535	480	430	375	(310)
Total flux	11 710 ±230	10 689 ±430	9242 ±600	8107 ±640	7014 ±670	5674 ±660	4789 ±630	4051 ±620	3237 ±580	2735 ±570	2313 ±530	1853 ±475

could introduce systematic errors in the determination of the all-particle spectrum. That is, however, not so serious because the contribution of heavy elements to the all-particle spectrum is not as dominant as the proton and helium components. This will be addressed again (see Table IX).

By summing up these curves, we obtain the all-particle spectrum as shown in Fig. 21 (heavy solid curve), where the dotted area corresponds to the region between the upper and lower limits shown in Fig. 19, and several individual elements are plotted together without distinguishing between observers (if necessary, see Figs. 19 and 20). We also plot the JACEE data [37] (※), the proton-satellite data [2] (×), and the air-shower data (+, ⋕ ; compiled by Nagano *et al.* [40]). One finds that our result is in agreement with the satellite data for $E_P \lesssim 50$ TeV/particle, while it deviates significantly from both the JACEE and the satellite data in the higher-energy region, even assuming the flux of the upper bound for our data.

Now, extrapolating our result to 10^{15}–10^{16} eV/particle, it seems that the air shower data gives a somewhat overestimation in the "knee" region, or we can say that the "knee" may not be as sharp as the air-shower people have predicted. One may comment that our estimation is based on extrapolation and we have no directly observed data there. We wish, however, to emphasize firmly that both Spacelab-2 and our data on the flux (multiplied by $E_P^{2.5}$) of heavy components show a *decreasing*

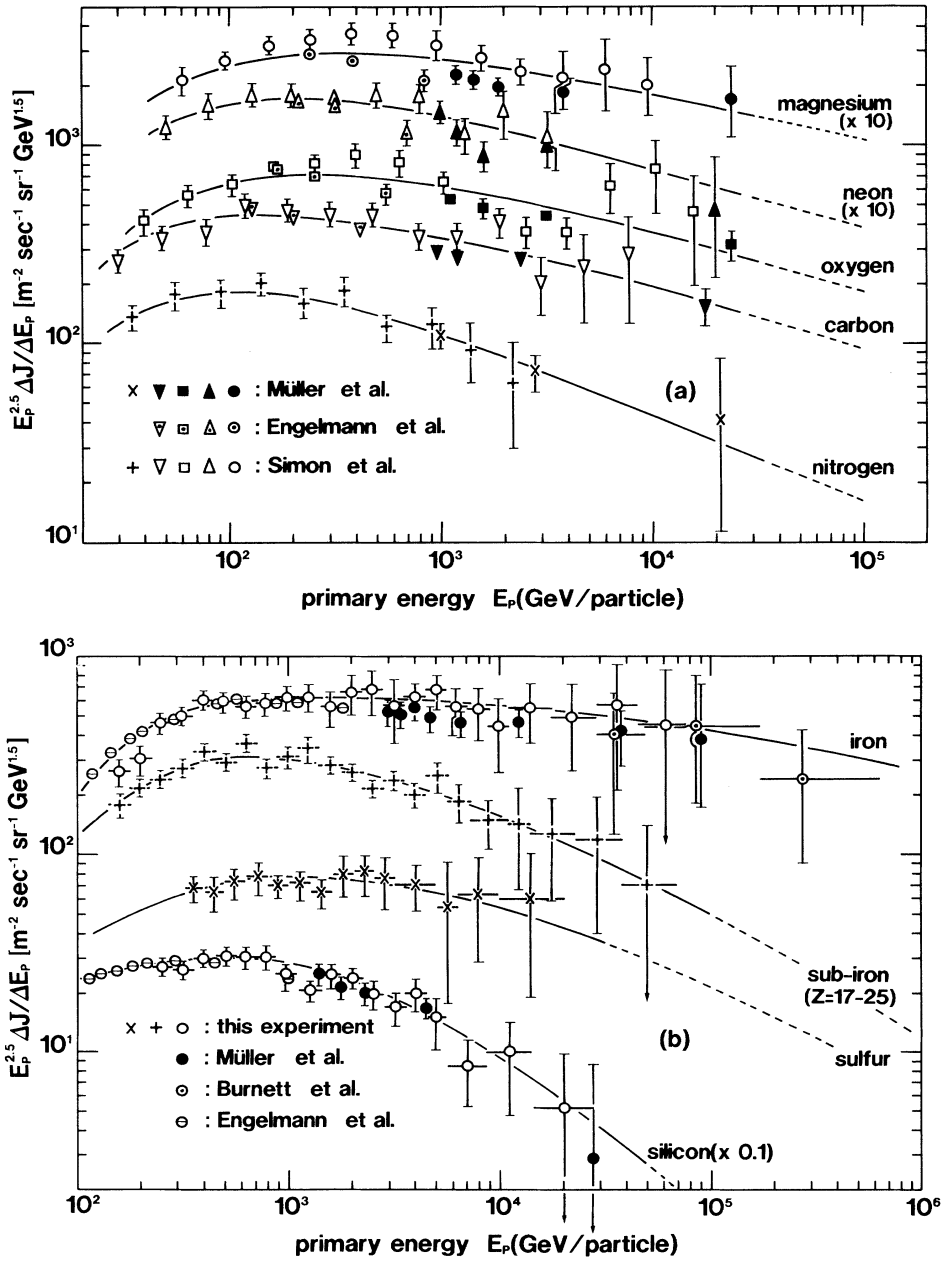

FIG. 20. Fluxes of (a) middle heavy group (carbon to magnesium), and (b) heavy group (silicon to iron). For the nitrogen data obtained by Müller *et al.*, we plot them by referring to the relative intensity shown in Ref. [46]. Curves for heavy group (b) are drawn by eye in order to sum up the fluxes of individual elements.

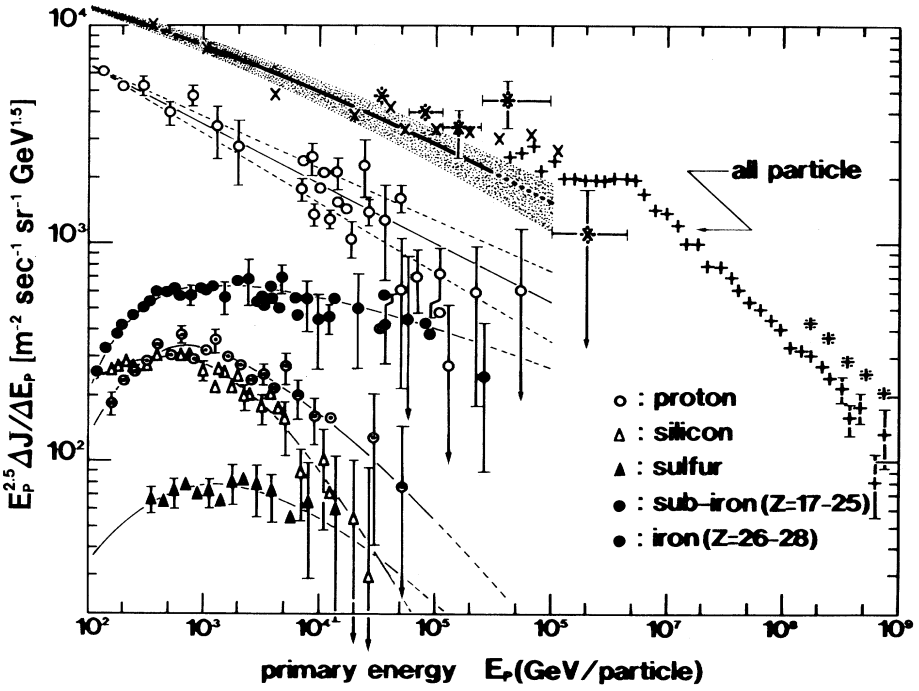

FIG. 21. All-particle spectrum obtained by summing up the flux of each element (Figs. 19 and 20), together with those by other groups, including air shower experiment. Thick solid curve is obtained by the superposition of the curves drawn in Figs. 19 and 20, and the dotted area corresponds to those inside the upper and lower broken lines in Fig. 19. ※ : Asakimori *et al.*; × : Grigorov *et al.*; +, ⁜ : compiled by Nagano.

tendency starting from somewhere in the energy region ~ 10 TeV/particle or less, instead of *growing* with increasing energy.

Until now, the "knee" has been interpreted as the contribution coming from, for instance, a drastic increase of heavy elements [41], or from a new source [42] consisting of singly charged element (or at most a mixture of singly and some doubly charged), different from the familiar source type giving normal cosmic-ray abundance. If so, such signals should appear already in the energy region of 10–100 TeV/particle. Otherwise we need either a sharp Gaussian-like contribution just near 10^{15} eV/particle, or something new and neutral not recorded in our detector. However, we have to wait a little longer to get a firm conclusion, since the direct observational data are very poor in the region $\gtrsim 50$ TeV/particle. In fact, the direct observational data scatter considerably among different observers in the high-energy region. For instance, the proton-satellite data give a much higher total flux than our data, and the JACEE data give still higher fluxes than the satellite data (see Fig. 21).

In this connection we would like to make one remark. The all-particle energy spectrum obtained by an air-shower array *at sea level* would involve some uncertainty around the "knee" region. The present large-scale air-shower arrays at sea level are principally designed aiming at the air showers of energies, for example, 10^{20-21} eV, where we might have the chance to observe the cosmic-ray energy cutoff, and, therefore, are not fully suited for observation of 10^{15} eV air showers. At sea level the latter showers are very old. Its most severe consequence is that their shower size estimation would include considerable uncertainty, because the flatness of their lateral distributions in their core regions might lead to critical core-location errors. Now, for the air showers initiated by $\sim 10^{15}$ eV/particle primaries, their respective shower maxima are reached at the atmospheric depth of 400–600 g/cm^2, depending on the mass number of the primaries. For this reason, it is highly desirable that more extensive study of air showers are carried out in the "knee" region by *high mountain altitude* experiments and that the comparison is made between the air-shower data and the direct observational data. It in turn would enhance, to a considerable extent, the reliability in the observation of air-shower sizes into absolute primary energies.

In Table IX, we give numerical flux values of individual elements obtained from the curves drawn in Figs. 19 and 20, where they are multiplied by $E_P^{2.5}$, and the unit is in m^{-2} s^{-1} sr^{-1} GeV$^{1.5}$ (E_P is in GeV/particle). The numerical values in the parentheses are those expected by extrapolating the curves to the higher energy. $\pm$ for proton and helium components denotes the upper and lower limits shown in Fig. 19.

D. Average mass of primary

Some observers [41,43] have reported that the abundances of lighter elements such as proton and helium decrease rapidly at higher energy, while heavier ones, particularly iron, increase considerably. One therefore expects the abundances might cross over with each other somewhere in the high-energy region.

We show the relative fluxes of typical elements to the total in Fig. 22, where, to avoid complexity, we do not discriminate the symbols of experimental points for different observers (if necessary, see Figs. 19 and 20). Though the proton fraction seems to decrease in the

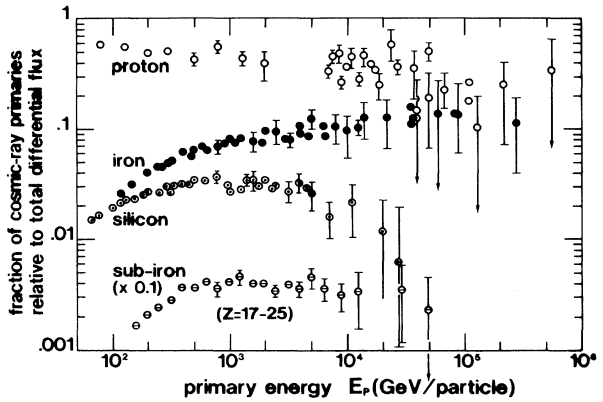

FIG. 22. Fraction of typical cosmic-ray elements relative to the total flux, where experimental points are not discriminated between different observers to avoid complexity (if necessary, see Figs. 19 and 20).

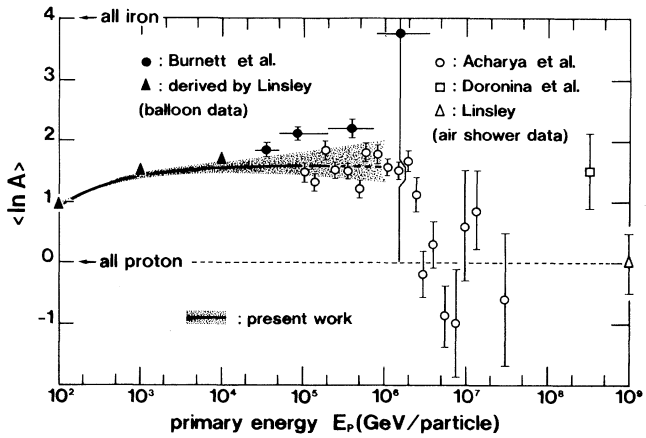

FIG. 23. Average value of $\ln A$ as a function of particle energy. Thick solid curve is our result obtained from Table IX, and the dotted area corresponds to those inside the upper and lower broken lines shown in Fig. 19.

higher-energy region $\gtrsim 100$ TeV, we wonder if the shower maximum is surely caught in the calorimeter with thickness of only 7–8 radiation lengths, the common thickness of balloon-borne emulsion chambers [3,4], for such a high-energy cascade shower, even if taking an elongation of path length due to an inclined projectile into account. If not, the proton fraction might be slightly larger than those plotted here. One should therefore keep such a possibility in mind.

One finds in Fig. 22 that the iron abundance increases gradually up to 100 TeV/particle, while others (even the sub-Fe component) shows a flattening or decreasing tendency with energy. Since the experimental points unfortunately fluctuate considerably in the high-energy region $\gtrsim 50$ TeV/particle, it seems difficult at this stage to conclude whether proton and iron components cross with each other or not. We can firmly say, however, that iron does not increase so drastically as to cover the excess in the "knee" region.

We present the average mass of cosmic-ray primaries as a function of particle energy together with other groups [44,45] in Fig. 23, where the vertical axis designates the average of the logarithm of the mass number. Our data (heavy solid curve) is obtained from Table IX, including those with parentheses. Though we make use of extrapolated data for middle heavy elements in the higher-energy region, the average value of $\ln A$ is dominantly influenced by proton, helium, and iron only, with energies reaching several hundred TeV/particle. The dotted area corresponds to the upper and lower limits often mentioned before.

One notes that the JACEE data and probably also the proton-satellite data give much higher flux values for heavy elements than ours, even assuming the upper limits in our data. Since the JACEE iron flux is nearly the same as those obtained by ours and the Spacelab-2 [see Fig. 20(b)], we expect that the abundance ratio of sub-iron to iron group will show a drastic increase in the higher-energy region, in contrast to the decreasing feature obtained by the present work (see Fig. 18). If it is to be the case, the JACEE data are going to indicate that, while in the lower-energy region the behavior of the sub-iron group is well reproduced by a leaky-box model with $\lambda_e \propto R^{-0.5}$ to $R^{-0.6}$, it deviates considerably from the prediction of the model in higher-energy region. Another choice of reasoning would be to assume the possibility that the above-mentioned behavior of the JACEE sub-iron group could be only apparent, and to seek for the problem either in the detection efficiency estimation ambiguity or in the energy estimation uncertainty. In any event, further mutual cross checks are quite desirable among different observers.

Though the air-shower data seems to agree with ours in the energy region 100–1000 TeV/particle, we have to first solve the discrepancy between our extrapolated data and the air-shower data in the "knee" region as shown in Fig. 21.

E. Summary and outlook

The present paper is focused mainly on the study of the procedure to obtain the absolute intensity of primaries, taking various effects into account, and to compare our results with those of previous observations. Several theoretical speculations on cosmic-ray propagation have been reported previously, and we would like to discuss the relation between our data and these models in a separate paper to appear shortly. In the following, we summarize our results, list the problems left to be solved and make note of speculations still under investigation.

(i) How well is the abundance ratio of the sub-Fe/Fe extending to TeV/N reproduced by a powerlike rigidity dependence of escape length $\lambda_e(R)$, in connection with the source abundances?

(ii) Can the rapid decrease of the silicon intensity in the higher-energy region $\gtrsim 100$ GeV/N can be reliably established? If so, what information or condition does it bring us for the source spectrum and/or the propagation in the interstellar medium?

(iii) Is the primary spectrum observed at the Earth completely explained by assuming rigidity spectra for individual elements with a common index $R^{-2-\delta}$ at a single kind of source alone? This question is closely related to (ii), if true.

(iv) It seems difficult at this stage to conclude definitely whether or not proton and iron intensities cross over with each other. We can say, however, that they do not cross at energies lower than ~ 100 TeV/particle.

(v) Our data suggests that the intensities of individual heavy elements, expressed in the form of $E_P^{2.5}\Delta J/\Delta E_P$, show decreasing tendencies somewhere already from the energy region ~ 10 TeV/particle, so the excess found in the "knee" region, if it actually exists, seems hard to understand in the framework of heavy dominant model.

(iv) What is the origin of the discrepancy between our extrapolated data and air-shower data of the all-particle spectrum in the "knee" region? Does this originate in our estimation method to sum up individual elements, or in the conversion process from air-shower size to primary energy (including the change of nuclear interaction), or in any new contributing components around the "knee"?

ACKNOWLEDGMENTS

We are much indebted to the staff of the balloon division of Institute of Space and Astronautical Science (ISAS), Sagamihara, Japan, for the successful flight and the recovery of our chamber. We also thank the staff of emulsion division of the Institute of Cosmic Ray Research (ICRR, University of Tokyo) for valuable discussions as well as their helpful processing work of sensitive materials. Thanks are also due to K. Yokoi (Aoyama-Gakuin University) and M. Nagano (ICRR) for their valuable discussions and comments. We acknowledge G. Dion (ICRR) for his careful reading of the present manuscript. This work was financially supported by ICRR (E40, 1989), and in part by ISAS (B50-31, 1989).

APPENDIX A: CONTRIBUTION OF WOUNDED PROTONS

The transverse momentum distribution of a leading proton in the process of proton-proton interaction is approximately given by [24]

$$\varphi(p_T) \propto e^{-p_T^2/p_0^2} \quad \text{with } p_0 \simeq 400-600 \text{ MeV}/c \ . \tag{A1}$$

We therefore write the distribution of the emission angle of wounded proton, corresponding to Eq. (9) in the text, as

$$\varphi_w(q)=a_w^2 e^{-a_w^2 q^2} \quad \text{with } a_w = M_N/\sqrt{2}\sigma_w . \tag{A2}$$

Denoting the average fractional momentum of the leading proton as $\langle x \rangle$, the relation between σ_w and p_0 is given by

$$p_0=\sqrt{2}\langle x \rangle \sigma_w \ , \tag{A3}$$

and setting $\langle x \rangle \simeq 0.5$, we get

$$\sigma_w \simeq 560-850 \text{ MeV}/c \ . \tag{A4}$$

Of course, σ_w fluctuates considerably event to event, which we regard as a free parameter.

Now, Eq. (9) is the angular distribution of fragments produced by the evaporation process, so that we put a subscript "ev" to φ:

$$\varphi_{\text{ev}}(q)=\tau_1 a_1^2 e^{-a_1^2 q^2}+\tau_2 a_2^2 e^{-a_2^2 q^2} \ . \tag{A5}$$

Since Eqs. (A2) and (A5) are both normalized to unity, the angular distribution of charged fragments including wounded protons is expressed by

$$\varphi(q)=N_{\text{ev}}\varphi_{\text{ev}}(q)+N_w\varphi_w(q) \quad \text{with } N_f=N_{\text{ev}}+N_w \ , \tag{A6}$$

where N_{ev} and N_w are the number of charged fragments $(p,\alpha,\text{Li},\ldots)$ produced by the evaporation process and the number of wounded protons, respectively, and N_f the total number of (charged) fragments including the wounded protons.

The number of fragment protons N_p, including both evaporated and wounded ones, is experimentally given by

$$N_p=Z_P-\sum_{k\geq\alpha} N_k Z_k \ , \tag{A7}$$

where Z_P and Z_k are the charges of a projectile nucleus and a fragment k heavier than the proton, respectively, and N_k the number of the fragment k. We can therefore experimentally obtain the total number of charged fragments as follows:

$$N_f=\sum_{k\geq\alpha} N_k+N_p=Z_P-\sum_{k\geq\alpha} N_k(Z_k-1) \ . \tag{A8}$$

Practically, however, we do not know the rate of N_w to N_{ev} for each event, so that we regard N_w as a free parameter in this step. Now, we have two free parameters (σ_w, N_w), and these two are determined by fitting Eq. (A6) to each event with use of the maximum-likelihood technique. In this case, the fitting curve is nonlinear, so that we need initial values for γ_L, σ_w, and N_w. The first (γ_L) is set with the value estimated from Eqs. (13) and (15) in the text, and the second (σ_w) with 707 MeV/c ($p_0=500$ MeV/c), and $N_w=0$ for the third. After setting these initial values, we can iteratively get the best values.

In Fig. 24, we demonstrate two examples of the fitting, where the projectiles are (a) silicon with an energy of $E_N=16.1$ GeV/N, and (b) iron with $E_N=1.51$ TeV/N, where the latter energy is the highest in the present observation. Fragmentation modes are $\text{Li}+2\alpha+7p$ for (a), and $F+17p$ for (b), respectively. In the case of (b), charged pions ($\sim 60\pi^{\pm}$'s in the forward cone in the c.m.s.) are also produced besides the fragment particles. Figure 25 shows the correlation between two energies, one estimated from Eq. (13) and the other corrected by the curve fitting mentioned above.

Through this work, we simultaneously get the three quantities, γ_L, σ_w, and N_w, and the latter two quantities are very interesting in the study of high-energy nucleus interactions. We will leave, however, the discussion to a

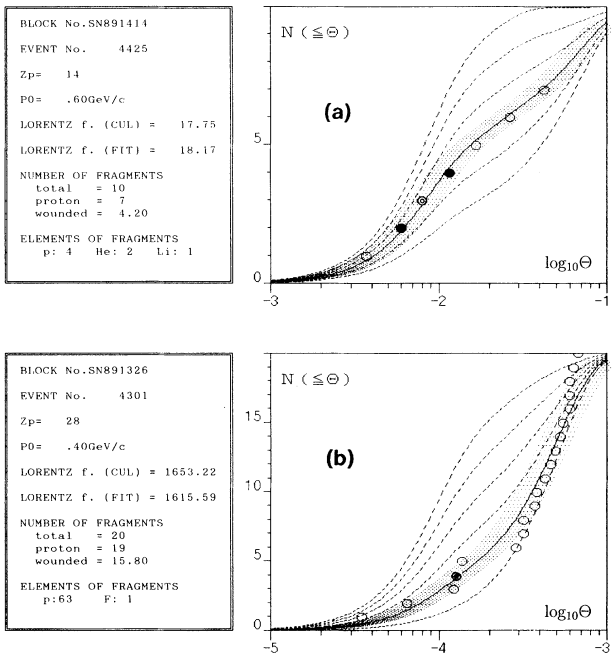

FIG. 24. Examples of curve fitting to fragment data, where several broken curves denote those changing the rate of wounded proton in the total fragment particles (p,α,Li, . . .), and dotted area means the uncertainty of the angular measurement, mainly coming from the determination of the primary axis ($\sim 15\%$). (b) is the highest-energy event obtained by the present observation. ○: proton; ●: α; ◎: lithium; ⊙: fluorine.

separate paper, because it deviates slightly from the present subject.

APPENDIX B: EXPLICIT FORM OF η_{ij}

We investigate here the explicit form of η_{ij} in several simple cases, which give, however, the principal contribution to the fragment process in the atmosphere.

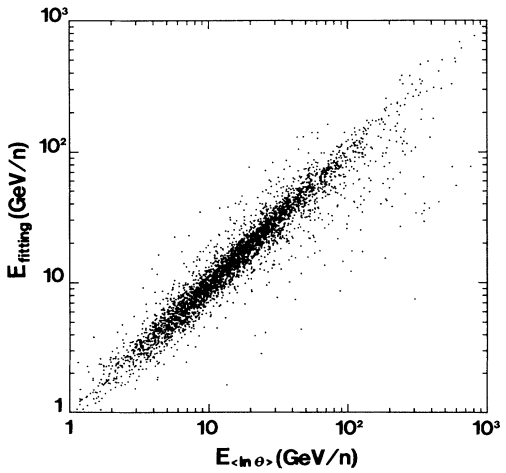

FIG. 25. Correlation between $E_{\langle \ln\Theta\rangle}$ and E_{fitting}, where the former is estimated by Eqs. (12) and (14), and the latter by the curve fitting, taking account of the wounded proton contribution.

First, let us consider a case that a primary nucleus i arrives at some observation level t without interaction; this is the case of $i=j$ in Eq. (23) in the text. In the case of a vertical incidence, it is given simply by

$$N_{i\to i,\perp}(t)=N_i^{(0)}e^{-t/\lambda_i} , \tag{B1}$$

(see Appendix C on the relation between the collision mean free path λ_i and the attenuation mfp Λ_i). Then we have immediately the following relation from Eqs. (B1), (21), and (22), taking the zenith-angle effect into account:

$$\begin{aligned} N_{i\to i}(t)&=\int\int_{\Omega\le 2\pi} N_{i\to i,\perp}(t/\cos\theta)\cos\theta\, d\Omega \\ &=S\Omega_{ii}(t)TI_i^{(0)}e^{-t/\lambda_i} , \end{aligned} \tag{B2}$$

where

$$\Omega_{ii}(t)=2\pi e^{t/\lambda_i}E_3(t/\lambda_i) , \tag{B3}$$

with

$$E_n(z)=\int_1^\infty \frac{1}{x^n}e^{-zx}dx . \tag{B4}$$

$\Omega_{ii}(t)$ is the effective solid angle at the observation level t, and $E_n(z)$ the exponential integral function with index n. Then, from Eqs. (B2), (22), and (23), we get

$$\eta_{ii}(t)=\Omega_{ii}(t)/\Omega_0=2e^{t/\lambda_i}E_3(t/\lambda_i) . \tag{B5}$$

That is, $\eta_{ii}(t)$ means the ratio of effective solid angle at the observation level t to that at top of the atmosphere ($=\pi$).

Second we consider a case that a nucleus j ($i>j$) arrives at level t through a one-step fragment process ($i\to j$) of the primary i. In the case of the vertical incidence, the number of primary i at level t' is given by replacing t by t' in Eq. (B1). Since the production rate of the nucleus j at $(t',t'+dt')$ is $P_{ij}dt'/\lambda_i$, and the attenuation rate of the nucleus j thus produced is $\exp[-(t-t')/\lambda_j]$ during the passage of $t-t'$ in air, we have

$$\begin{aligned} N_{i\to j,\perp}(t)&=\int_0^t N_{i\to i,\perp}(t')\frac{dt'}{\lambda_i}P_{ij}e^{-(t-t')/\lambda_j} \\ &=N_{i\to i,\perp}(t)\frac{t}{\lambda_i}P_{ij}G\left[\frac{t}{\lambda_{ij}}\right] , \end{aligned} \tag{B6}$$

where

$$G(x)=\frac{e^x-1}{x} \quad \text{with} \quad \frac{1}{\lambda_{ij}}=\frac{1}{\lambda_i}-\frac{1}{\lambda_j} . \tag{B7}$$

Similarly as in the case of Eq. (B2), taking the zenith-angle effect into account, we get, immediately from Eq. (B6),

$$\begin{aligned} N_{i\to j}(t)&=\int\int_{\Omega\le 2\pi} N_{i\to j,\perp}(t/\cos\theta)\cos\theta\, d\Omega \\ &=S\Omega_{ij}(t)TI_i^{(0)}e^{-t/\lambda_i}(t/\lambda_i)P_{ij} , \end{aligned} \tag{B8}$$

where

$$\Omega_{ij}(t)=2\pi e^{t/\lambda_i}E_{ij}(t)\ , \tag{B9}$$

with

$$E_{ij}(t)=\left[E_3\left[\frac{t}{\lambda_j}\right]-E_3\left[\frac{t}{\lambda_i}\right]\right]\Big/\frac{t}{\lambda_{ij}}$$
$$\simeq E_2\left[\frac{t}{\lambda_j}\right]-\frac{1}{2}\frac{t}{\lambda_{ij}}E_1\left[\frac{t}{\lambda_j}\right]\ . \tag{B10}$$

Here we used an approximation, $1/\lambda_{ij}\ll 1/\lambda_i,\ 1/\lambda_j$, which is satisfactory for the practical purpose.

Finally, from Eqs. (B8), (22), and (23), we obtain

$$\eta_{ij}(t)=\frac{t}{\lambda_i}P_{ij}\frac{\Omega_{ij}(t)}{\Omega_0}=\frac{t}{\lambda_i}P_{ij}2e^{t/\lambda_i}E_{ij}(t)\ . \tag{B11}$$

That is, in the case of the one step process, $\eta_{ij}(t)$ is given by a reasonable form:

(collision probability $\equiv t/\lambda_i$)

$\times$(fragmentation rate $\equiv P_{ij}$)

$\times$(solid angle term) .

APPENDIX C: ATTENUATION LENGTH OF HEAVY PRIMARY

As is well known, if a nuclear interaction is not catastrophic as in the case of protons, we can distinguish strictly two kinds of mean free paths, the collision mfp λ and the attenuation mfp Λ, and we have a well-known relation between them given by

$$\frac{1}{\Lambda}=\frac{1-\langle(1-K)^{\beta}\rangle}{\lambda}\ , \tag{C1}$$

where β is the integral spectral index of primary proton and K is the inelasticity of the proton interaction. On the other hand, in the case of heavy primaries, most of the projectile nuclei suffer the charge transition ΔZ in collision with the air target, so that the interaction is catastrophic (except the diffractive-type interaction) in the sense we follow the primary nucleus with charge Z_P alone, leading to $\lambda\simeq\Lambda$.

However, in a case that only neutron fragments are produced in the nuclear interaction ($\Delta Z=0, \Delta A\neq 0$), we regard the survival nucleus as the same with the projectile; i.e., it seems for us as if no nuclear interaction actually has occurred. This means that the attenuation mfp looks elongated, i.e., explicitly writing

$$\frac{1}{\Lambda_i}=\frac{1-P_{ii}}{\lambda_i}\ , \tag{C2}$$

where P_{ii} denotes the probability of neutron emission without any proton emission [5–10 % (Ref. [30]).

Now, another point we have to take into consideration in the case of heavy primary observation is the charge resolution σ_i of the track detector we use. That is, while we showed an example of $\Delta Z=0$ with $\Delta A\neq 0$ in the above, it seems again as if no nuclear interaction has occurred in the case of $\Delta Z\simeq\sigma_i$, even if a spallation reaction actually occurred somewhere high above the detector. We investigate here the internal relations among λ_i, Λ_i, σ_i, and P_{ij} with $\Delta Z\simeq\sigma_i$.

Equation (C2) is derived from the equation

$$\Delta N_i=-\frac{\Delta t}{\lambda_i}N_i+\frac{\Delta t}{\lambda_i}N_iP_{ii}\ . \tag{C3}$$

Here, let us consider a practical observation. As is shown in Table III, in order to select some primary species i with a charge of Z_i, we set the charge range $Z_{\min}\sim Z_{\max}$ (usually, $Z_{\min}=Z_i-\sigma_i$, and $Z_{\max}=Z_i+\sigma_i$), and pick up those within the range. So, P_{ii} in Eq. (C3) should be replaced by

$$V_i=s_0P_{ii}+s_1P_{ii-1}+\cdots\ , \tag{C4}$$

where

$$s_k=\int_{Z_{\min}}^{Z_{\max}}e^{-(Z-Z_{i-k})^2/2\sigma_{i-k}^2}\frac{dZ}{\sqrt{2\pi}\sigma_{i-k}}\ . \tag{C5}$$

Evaluating explicitly the values $s_0, s_1, \ldots$ and using Table III for iron and silicon primaries, we obtain

$$s_0=0.828\ ,\quad s_1=0.499\ ,\quad s_2=0.129\quad \text{for Fe}\ , \tag{C6a}$$

$$s_0=0.742\ ,\quad s_1=0.118\ ,\quad s_2=0.001\quad \text{for Si}\ . \tag{C6b}$$

Equation (C4) is therefore written in good approximation as

$$V_i\simeq s_0P_{ii}+s_1P_{ii-1}\ ; \tag{C7}$$

i.e.,

$$\frac{1}{\Lambda_i}=\frac{1-V_i}{\lambda_i}\ . \tag{C8}$$

The attenuation mfp is easily obtained from the zenith-angle distribution in our experiment. Since the path length in the atmosphere is $t_0/\cos\theta$ for a cosmic-ray primary with the zenith angle θ (t_0 is the observation level), we can get a depth-intensity relation for individual elements. In Fig. 26, we show the depth-intensity relation for iron (open circle) and silicon (closed circle), together with straight lines obtained by the least sum of the squares method. One finds that both slopes give slightly larger than those expected from the collision mfp (broken straight lines), justifying the above considerations.

From Fig. 26, we get

$$V_{\mathrm{Fe}}=0.129\pm 0.015\ ,\quad V_{\mathrm{Si}}=0.082+00.012\ . \tag{C9}$$

Conversely, from Eqs. (C7)–(C9), we can estimate the fragmentation probabilities for small charge transitions, P_{ii}, P_{ii-1} ($\Delta Z=0$, 1, respectively), with use of the elongation in the attenuation mfp. It is, however, difficult to get both independently; instead we estimate here the average of the two:

$$\langle P_{\Delta Z=0,1}\rangle=\frac{P_{ii}+P_{ii-1}}{2}=\frac{1+\omega}{s_1+s_0\omega}\frac{V_i}{2}$$
$$\text{with}\ \omega=P_{ii}/P_{ii-1}\ . \tag{C10}$$

Heavy-ion data [29,30] suggest $\omega=0.5-1$, though the

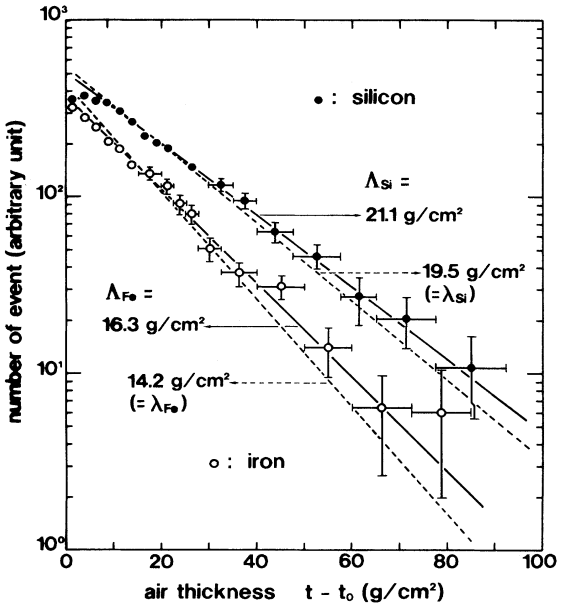

FIG. 26. Depth-intensity relation of iron and silicon components obtained by the zenith-angle distribution. t_0 denotes the observation level ($=11.7$ g/cm^2). Solid straight lines are obtained by the sum of the least-squares method, and the broken lines corresponding to the collision mean free paths (see Table V in text).

fluctuations are considerable. Equation (C10) depends, fortunately, on rather weakly ω, so that we do not seriously worry about the choice of ω, and get

$$\langle P_{\Delta Z=0,1}\rangle = \begin{cases} 0.097-0.106 & \text{for Fe}, \quad \text{(C11a)} \\ 0.095-0.126 & \text{for Si}. \quad \text{(C11b)} \end{cases}$$

Open circles in Figs. 13(a) and 13(b) are thus obtained.

Again one should keep in mind that the attenuation length of heavy primaries in the atmosphere depends on the resolution of the charge determination. For instance, in our case ($\sigma_{Fe}=0.97$ and $\sigma_{Si}=0.46$), we have $\Lambda_{Fe}=16.3$ g/cm^2 and $\Lambda_{Si}=21.1$ g/cm^2. On the other hand, if one determines the charge with $\sigma_i \simeq 0$, and monitors neutron fragments together produced by heavy-primary spallation in air, one would surely find $\Lambda_i \simeq \lambda_i$.

APPENDIX D: CONTAMINATION OF SECONDARY FRAGMENTS

Equation (26) for the j component is rewritten as

$$I_j^{(\text{obs})} = H_{jj}(t) I_j^{(0)} + \sum_{i>j} H_{ij}(t) I_i^{(0)} . \quad \text{(D1)}$$

The first term in the right-hand side corresponds to the *primary* j component arriving directly at our chamber, and the second to the *secondary* j component coming from the spallation reaction of heavier components i (mostly from iron), where the fragmentation parameter P_{ij} is of course included in the latter H_{ij} [see Eqs. (27) and (B11)].

Setting

$$\Delta I_j^{(\text{frag})} = \sum_{i>j} H_{ij}(t) I_i^{(0)} ,$$

let us estimate its contamination rate to the observed flux $I_j^{(\text{obs})}$, expressed by

$$\frac{\Delta I_j^{(\text{frag})}}{I_j^{(\text{obs})}} = \frac{\epsilon_j}{1+\epsilon_j} \quad \text{with } \epsilon_j = \sum_{i>j} H_{ij} I_i^{(0)} / H_{jj} I_j^{(0)} . \quad \text{(D2)}$$

Defining the relative intensity of the primary i to the primary j as $r_{ij}=I_i^{(0)}/I_j^{(0)}$, we obtain, from Eqs. (27), (B5), (B10), and (B11),

$$\epsilon_j(t) = \sum_{i>j} P_{ij} r_{ij} F_{ij}(t) , \quad \text{(D3)}$$

where

$$F_{ij}(t) = \frac{t}{\lambda_i}\left[E_2\left[\frac{t}{\lambda_j}\right] - \frac{1}{2}\frac{t}{\lambda_{ij}} E_1\left[\frac{t}{\lambda_j}\right]\right] \Big/ E_3\left[\frac{t}{\lambda_j}\right] . \quad \text{(D4)}$$

In Fig. 27, we show the numerical values of $F_{ij}(t)$ for several choices of i and j at three observational levels. One therefore finds they are almost constant, irrespective of the kind of primary species i, for instance, approximately as large as 0.7–1.0 at our observational level, ~ 10 g/cm^2.

To estimate practically the contamination rate, $\Delta I_j^{(\text{frag})}/I_j^{(\text{obs})}$, we first calculate the iron primary flux $I_{Fe}^{(0)}[\simeq I_{Fe}^{(\text{obs})}/H_{FeFe}(t)]$ with $\Delta I_{Fe}^{(\text{frag})} \simeq 0$ in Eq. (D2) because of $I_{Fe}^{(0)} \gg I_i^{(0)}$ ($i=$Co, Ni, . . .). Next we subtract successively the contamination of secondary fragments in subsequent heavy elements ($j=$Mn, Cr, . . .) with use of the fragmentation parameter P_{ij}, coming from the break-

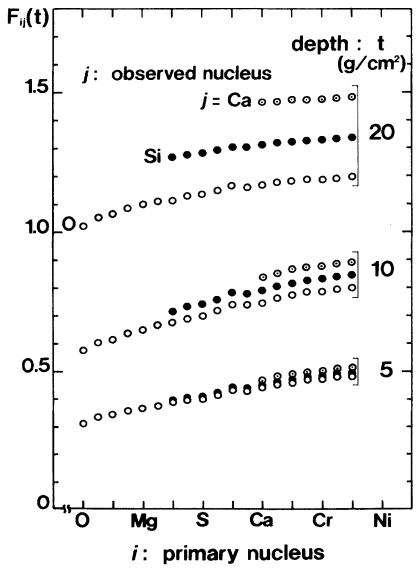

FIG. 27. Numerical values of $F_{ij}(t)$ for several sets of i and j at three observational levels.

TABLE X. Numerical results of the contamination rate of secondary fragments in the observed primary flux for several elements at three energy ranges, ≤ 10 GeV/N, 10–100 GeV/N, and 100–1000 GeV/N.

Primary j	E_0 (GeV/N) ≤ 10	$\Delta I_j^{(\mathrm{frag})}/I_j^{(\mathrm{obs})}$ $=10-100$	$=100-1000$
Iron	~0	~0	~0
Calcium	0.250	0.285	0.252
Argon	0.373	0.399	0.333
Sulfur	0.179	0.206	0.146
Silicon	0.040	0.051	0.061
17–20	0.313	0.380	0.345
21–25	0.350	0.464	0.434

up of a heavier i primary than the j primary (mostly from the iron spallation).

We summarize the numerical results of $\Delta I_j^{(\mathrm{frag})}/I_j^{(\mathrm{obs})}$ for typical elements in Table X, and find that the contamination rates are negligible for silicon, and 15–25 % for sulfur and calcium, while 30–45 % for other sub-iron groups. It shows that the estimation of the true flux $I_j^{(0)}$ depends rather strongly on the fragmentation parameter P_{ij} for a rare element such as argon and for sub-iron groups. So let us see the effect of the uncertainty of P_{ij} to the true flux.

From Eq. (D3), we get

$$\Delta\epsilon_j \equiv \frac{\Delta I_j^{(0)}}{I_j^{(0)}} \simeq -\frac{\Delta P_{ij}}{\langle P_{ij}\rangle}\epsilon_j \ , \tag{D5}$$

and because of $\epsilon_j \sim 1$ for rare elements [see Eq. (D2) and Table X], we find that the uncertainty of the true flux, $\Delta I_j^{(0)}/I_j^{(0)}$, is nearly equivalent to that of the fragmentation parameter:

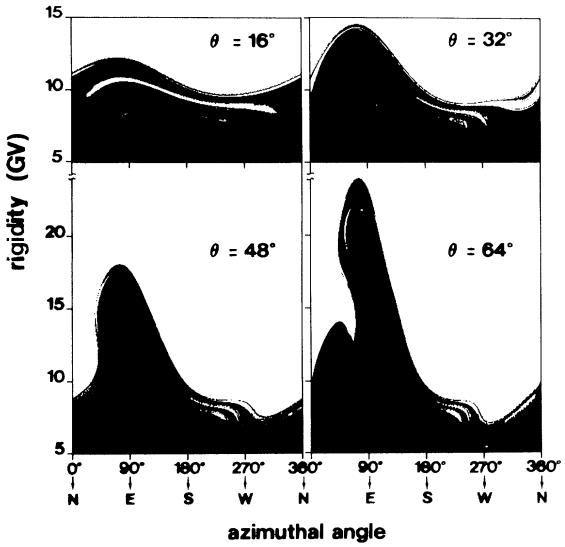

FIG. 28. Cutoff rigidity at Sanriku latitude [39.16°, 141.83°] for four cases of zenith angle as a function of azimuthal angle. While black area corresponds to the forbidden region for arriving cosmic ray, the white one corresponds to the allowed region.

$$\frac{\Delta I_j^{(0)}}{I_j^{(0)}} \simeq -\frac{\Delta P_{ij}}{\langle P_{ij}\rangle} \ . \tag{D6}$$

Now, recalling $\Delta P_{ij}/\langle P_{ij}\rangle \simeq 15-25$ % as shown in Fig. 13(a), one has to expect that the abundance ratios shown in Figs. 17(b) and 18 includes the uncertainty of 15–25 %.

APPENDIX E: SUMMARY OF CUTOFF RIGIDITY AT SANRIKU

The basic equation is given by the well-known equation

$$\frac{d\mathbf{R}}{dt} = \mathbf{v}\times\mathbf{B} \ , \quad \mathbf{R} = \text{rigidity of heavy primary} \ , \tag{E1}$$

TABLE XI. Numerical values of effective cutoff rigidity at Sanriku latitude with $[N,E]=[39.16°, 141.83°]$ for several arrival directions. The unit is GV.

θ \ φ	0° (North)	30°	60°	90° (East)	120°	150°	180° (South)	210°	240°	270° (West)	300°	330°
0°	10.34	10.40	10.43	10.43	10.43	10.38	10.38	10.38	10.37	10.36	10.36	10.35
6°	10.41	10.66	10.82	10.88	10.73	10.54	10.34	10.14	10.02	10.02	9.95	10.13
12°	10.27	10.86	11.36	11.42	11.13	10.59	10.14	9.72	9.67	9.70	9.72	9.84
18°	11.04	11.85	11.99	11.96	11.60	10.80	10.10	9.61	9.26	9.23	9.36	10.30
24°	11.04	12.30	13.09	13.04	12.24	11.06	10.00	9.38	8.97	9.10	9.51	10.03
30°	10.43	12.75	13.99	13.89	12.79	11.23	9.85	9.18	8.74	8.77	9.14	9.27
36°	9.42	13.04	14.99	14.88	13.47	11.47	9.83	9.04	8.70	8.62	8.42	8.32
42°	8.84	11.94	16.20	16.15	14.19	11.69	9.80	8.92	8.40	8.52	7.99	7.93
48°	8.73	10.00	17.68	17.59	15.07	11.92	9.70	8.61	8.34	8.24	7.50	7.72
54°	8.99	10.00	19.46	19.36	16.03	12.17	9.65	8.57	8.22	7.83	7.34	8.04
60°	9.29	11.00	14.85	21.44	16.80	12.44	9.60	8.48	8.23	7.43	7.14	8.08
66°	11.15	14.75	19.22	24.07	17.97	12.60	9.60	8.62	8.04	7.10	7.40	8.22
72°	14.20	19.12	26.90	27.31	19.06	12.84	9.54	8.51	7.86	6.85	7.38	8.66
78°	17.65	24.45	30.46	31.47	19.74	13.00	9.49	8.54	7.92	6.90	7.62	10.50
84°	21.90	30.62	34.97	36.62	20.05	12.95	9.54	8.64	8.24	7.05	7.52	13.00
90°	27.30	39.05	46.80	46.71	35.11	12.70	9.70	8.54	8.13	7.15	7.87	15.80

where $\mathbf{B}(r,\theta,\phi)$ is the magnetic field of the Earth. We solve Eq. (E1) by the use of Runge-Kutta-Gill method, details of which are presented in Ref. [47].

In Fig. 28, we show some examples of numerical results on the cutoff rigidity as a function of azimuthal angle for several choices of the zenith angle, where the black area means the forbidden region for cosmic-ray heavy primary to arrive at our chamber. One finds that there are many fine structures of penumbra, which have never been detected so clearly in past calculations. This is due to the numerical method with fine step width for θ and ϕ.

On the basis of these numerical results, we can obtain the effective cutoff momentum for various arriving directions (θ,ϕ), taking the effect of primary spectrum into account. In Table XI, we present a part of effective cutoff rigidity (in GV) in a large amount of numerical values. Practically, of course, we have stored on hard disk all of the numerical data with the step, $\Delta\theta=2°$ and $\Delta\phi=1°$, and performed a simulation calculation.

[1] For example, I. W. Axford, in *Proceedings of the 17th International Cosmic Ray Conference,* Paris, France, 1981 (Centre d'Etudes Nucléaires de Saclay, Gif-sur-Yvette, 1981), Vol. 12, p. 155.

[2] N. L. Grigorov, I. D. Rapoport, I. A. Savenko, V. E. Nesterov, and V. L. Prokhin, in *Proceedings of the 12th International Cosmic Ray Conference,* Hobart, Tasmania, 1971, Conference Papers, edited by A. G. Fenton and K. B. Fenton (University of Tasmania Press, Hobart, Tasmania, 1971), Vol. 5, pp. 1746, 1752, and 1760.

[3] T. H. Burnett *et al.*, Nucl. Instrum. Methods A **251**, 583 (1986).

[4] Y. Kawamura *et al.*, Phys. Rev. D **40**, 729 (1989).

[5] T. Fujinaga, M. Ichimura, Y. Niihori, and T. Shibata, Nucl. Instrum. Methods A **276**, 317 (1989).

[6] J. J. Engelmann, P. Goret, E. Juliusson, L. Koch-Miramond, N. Lund, P. Masse, I. L. Rasmussen, and A. Soutoul, Astron. Astrophys. **148**, 12 (1985).

[7] D. Müller, S. P. Swordy, P. Meyer, J. L'Heureux, and J. M. Grunsfeld, Astrophys. J. **374**, 356 (1991).

[8] Y. Kawamura *et al.*, in *Proceedings of the 21st International Cosmic Ray Conference,* Adelaide, Australia, 1990, edited by R. Protheroe (Graphic Services, Northfield, South Australia, 1990), Vol. 3, p. 89.

[9] M. Ichimura *et al.*, Nucl. Instrum. Methods A **300**, 374 (1991).

[10] M. Ichimura, Ph.D. thesis, Aoyama Gakuin University, 1992 (unpublished).

[11] M. Ichimura, K. Kirii, and T. Shibata, Nucl. Instrum. Methods A **300**, 616 (1991).

[12] M. Kitazawa, Master's thesis, Aoyama Gakuin University, 1991 (unpublished).

[13] M. Ichimura *et al.*, in *Proceedings of the 23rd International Cosmic Ray Conference,* Calgary, Canada, 1993, Conference Papers, edited by D. A. Leahy (University of Calgary, Calgary, 1993), Vol. 1, p. 591.

[14] M. F. Kaplon *et al.*, Phys. Rev. **85**, 296 (1952).

[15] Y. Sato *et al.*, Lett. J. Phys. Soc. Jpn. **54**, 4502 (1985).

[16] A. S. Goldhaber, Phys. Lett. **53B**, 306 (1974).

[17] H. Feshbach and K. Huang, Phys. Lett. **47B**, 300 (1973).

[18] For example, J. Hüfner, Phys. Rep. **125**, 129 (1985).

[19] H. Fukushima *et al.*, Phys. Rev. C **44**, 834 (1991).

[20] S. Tasaka *et al.*, J. Phys. Soc. Jpn. **54**, 3289 (1985); see also Ref. [15].

[21] K. B. Bhalla *et al.*, in *Proceedings of 5th High Energy Heavy Ion Study,* Berkeley, California, 1981 (LBL Report No. LBL-12652, Berkeley, 1981).

[22] H. Nanjo *et al.* (unpublished).

[23] H. G. Baumgart *et al.*, J. Phys. G **7**, 175 (1981).

[24] J. Whitemore, Phys. Rep. **27**, 187 (1976).

[25] C. Castagnoli *et al.*, Nuovo Cimento **10**, 1261 (1953).

[26] F. A. Hagen *et al.*, Astrophys. J. **212**, 262 (1977).

[27] P. J. Karol, Phys. Rev. C **11**, 1203 (1975).

[28] P. S. Freier and C. J. Waddington, Astrophys. Space Sci. **38**, 419 (1975).

[29] G. D. Westfall *et al.*, Phys. Rev. C **19**, 309 (1979).

[30] W. R. Webber *et al.*, Phys. Rev. C **41**, 533 (1990).

[31] E. M. Friedlander *et al.*, Phys. Rev. C **27**, 1489 (1983).

[32] C. H. Tsao and R. Silberberg, in *Proceedings of the 18th International Cosmic Ray Conference,* Bangalore, India, 1983, edited by N. Durgaprasad *et al.* (Tata Institute of Fundamental Physics, Bombay, 1983), Vol. 2, p. 194.

[33] M. Ichimura *et al.*, in *Proceedings of the Balloon Symposium,* edited by J. Nishimura (Institute of Space and Astronautical Science, Sagamihara, Japan, 1991), p. 153.

[34] A. Inoue, M. Wada, and I. Kondo, Bull. Inst. Sci. Ballooning **1**, 79 (1981).

[35] M. Simon *et al.*, Astrophys. J. **239**, 712 (1980).

[36] J. J. Engelmann *et al.*, in *Proceedings of the 18th International Cosmic Ray Conference* [32] Vol. 2, p. 17; W. R. Binns *et al.*, Astrophys. J. **324**, 1106 (1988); M. Garcia-Munoz *et al.*, Astrophys. J. Lett. **280**, 13 (1984); J. E. Grove *et al.*, Astrophys. J. **377**, 680 (1991); see also references quoted in Refs. [6,7,35].

[37] K. Asakimori *et al.*, in *Proceedings of the 22nd International Cosmic Ray Conference,* Dublin, Ireland, 1991, edited by M. Cawley *et al.* (Dublin Institute for Advanced Studies, Dublin, 1991), Vol. 2, p. 57.

[38] I. P. Ivanenko *et al.*, in *Proceedings of the 21st International Cosmic Ray Conference* [8], Vol. 6, p. 77.

[39] M. J. Ryan, J. F. Ormes, and V. K. Balasubrahmanyan, Phys. Rev. Lett. **28**, 985 (1972).

[40] M. Nagano *et al.*, J. Phys. G **10**, 1295 (1984).

[41] H. T. Freudenreich *et al.*, in *Proceedings of the 21st International Cosmic Ray Conference* [8], Vol. 9, p. 56.

[42] J. Linsley, in *Proceedings of the 18th International Cosmic Ray Conference* [32], Vol. 12, p. 135.

[43] Fuji-Kanbala ECC group, Phys. Rev. D **38**, 1404 (1988); **38**, 1417 (1988); **38**, 1426 (1988).

[44] B. Acharya *et al.*, in *Proceedings of the 18th International Cosmic Ray Conference* [32], Vol. 9, p. 191.

[45] I. V. Doronina *et al.*, in *Proceedings of the 21st International Cosmic Ray Conference* [8], Vol. 6, p. 150.

[46] D. Müller *et al.*, in *Proceedings of the 20th International Cosmic Ray Conference,* Moscow, USSR, 1987, edited by V. A. Kozyarivsky *et al.* (Nauka, Moscow, 1987), Vol. 4, p. 5.

[47] S. Somemiya, D. Kato, T. Ohsima, T. Shibata, and M. Ichimura, in *Proceedings of the Balloon Symposium* [33], p. 160.

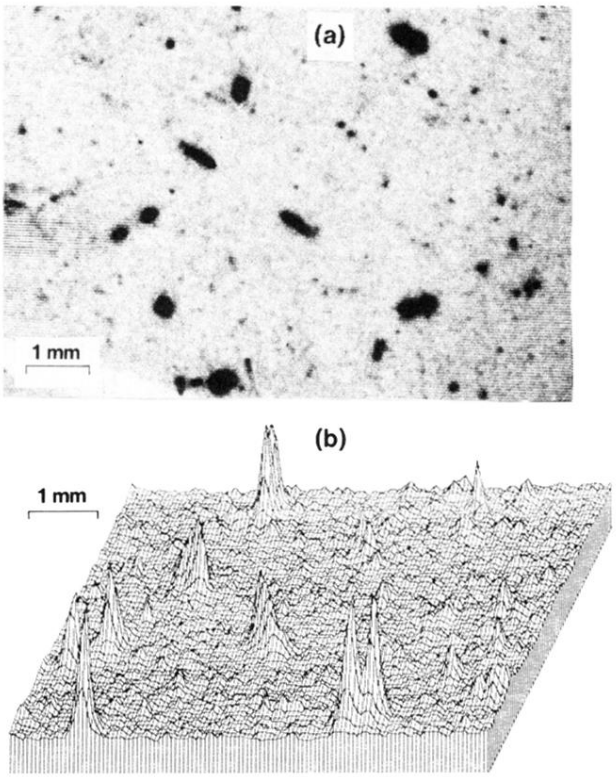

FIG. 2. Photograph of cosmic-ray heavy primaries recorded on x-ray film, (a) taken from the TV monitor and (b) the three-dimensional darkness contour map corresponding to the photograph.